PhD Thesis

ADVANCEMENTS IN NUCLEAR WASTE ASSAY

Debbie Curtis

Supervisor: Dr. M. Wormald

Supervisor: Dr. P. Norman

Academic Years 2004-2007

UNIVERSITY OF BIRMINGHAM

CANBERRA

ABSTRACT

The research described in this thesis is directed at advancing the state of the practice of the non-destructive gamma-ray assay of nuclear waste containers. A number of potentially accuracy-limiting issues were identified and addressed, resulting in new developments which were implemented on an instrument prior to entering it into service.

A set of Pu reference sources used for experimental data have been studied to determine the internal composition (density and fill height) of the sources to assist with validation of a point kernel model. This model has been used to observe the behaviour of gamma-rays in lumps of fissile material from plutonium over the mass range 0.001g to 350g, for a number of densities corresponding to Pu, PuO_2 and PuF_3. Established lump corrections have been analysed and have been found to produce large over- and under-corrected results for the range of masses. Due to the inadequacies of current techniques, a new Pu self-absorption correction method has been developed using the data from numerical simulations, allowing nature to reveal the correlations rather than traditional approaches based upon approximate models. For a 25g 1cm-high Pu flat-plate of density 15g.cm^{-3}, the developed Pu correction produces a result of (24.9 ± 8.8)g compared to (19.5 ± 0.9)g for the Fleissner 2-line method, and (14.7 ± 0.4)g for the Infinite Energy Extrapolation method.

The developed Pu correction method has been extended to the application of uranium lumps in waste matrices, provided the enrichment of the sample is known or may be determined via sophisticated isotopic analysis methods such as MGAU or FRAM. The U self-absorption correction method has been found to produce results within 30% of the true mass of the sample for the lumps studied.

An analysis of 'real drum' effects has been performed, including the revisiting of the Total Measurement Uncertainty (incorporating the uncertainty components of the new Pu and U self-absorption corrections) and results from known sources placed in artificial inhomogeneous waste matrices assayed inside a Canberra Auto Q2 system.

CONTENTS

FIGURES

TABLES

NOMENCLATURE

BEGe - Broad Energy Germanium detector

CSN - Count Sequence Number

DMSS - Dual Multi-Spectrum Scaling

DU - Depleted uranium (<0.7% ^{235}U) i.e. less than the natural abundance of ^{235}U

FRAM - Fixed-Energy Response Function Analysis with Multiple Efficiency, an isotopics software code

FWHM - Full Width Half Maximum

GAA - Genie 2000's Gamma Acquisition and Analysis program

Ge(Li) - Lithium drifted germanium

HDPE - High Density Polyethylene

HEU - High enrichment uranium (~93% ^{235}U)

HPGe - High purity Germanium

HLW - High Level Waste

HTGR - High Temperature Gas Reactor

IAEA - International Atomic Energy Agency

IEE - Infinite Energy Extrapolation method

IEU - Intermediate enrichment uranium (~40% ^{235}U)

ILW - Intermediate Level Waste

ISOCS - Canberra's *In Situ* Object Counting System/Software

LANL - Los Alamos National Laboratory

LLW - Low Level Waste

MCNP - Monte Carlo N-Particle transport code developed by LANL

MDA - Minimum Detectable Activity

MGA - Multiple Group Analysis, an isotopics software code

MGAU - Multiple Group Analysis for Uranium, an isotopics software code

NaI(Tl) - Thalium activated sodium iodide

NDA2000 - Canberra's waste assay software for the Genie 2000 family of systems

NDE - Non-Destructive Examination

NID	- Nuclide Identification
Nirex	- Nuclear Industry Radioactive Waste Executive
NUDS	- Non-Uniformity Detection Software
PDT	- Pacific Daylight Time
PNCC	- Passive Neutron Coincidence Counter
$^{240}Pu_{eff}$	- The effective ^{240}Pu mass of a sample from PNCC assay. ^{240}Pu is typically the primary source of fission neutrons from Pu in the fuel cycle
R^2	- A statistical measure between 0 and 1 indicating how well a regression line approximates to data points
ROI	- Region of Interest in a gamma spectrum
RTR	- Real Time Radiography
SAC	- Self-Absorption Correction
SAF	- Self-Absorption Factor
SGS	- Segmented Gamma-Ray Scanner
SILWAS	- Solid ILW Assay System
SNM	- Special Nuclear Material
TGS	- Tomographic Gamma Scanner
TMU	- Total Measurement Uncertainty
VLLW	- Very Low Level Waste
VWA	- Volume Weighted Average
Z	- Atomic number

1 INTRODUCTION

This work addresses a number of issues with current gamma techniques for Non-Destructive Assay (NDA) of nuclear waste. Modelling is used to form an understanding that leads to improve algorithms and correction methodologies, with the aim of advancing the science of NDA.

1.1 Background

1.1.1 What is Nuclear Waste?

Nuclear Waste is defined as: "any material contaminated by or incorporating radioactivity above thresholds defined in legislation is known as radioactive waste." [1]. It originates from a number of different sources such as power stations, nuclear weapons processing, hospitals, science laboratories etc, in a number of chemical forms and has four main types in the International Atomic Energy Authority [2]: high, intermediate, low and very low level wastes [3].

High level waste (HLW) consists mainly of spent fuel and waste from reprocessing of nuclear fuels in liquid form. High level waste is highly radioactive and consequently has a high thermal power output (typically greater than $2kW/m^3$) which must be taken into account for storage and hence must be stored behind appropriate shielding. It can be made into solid glass waste through the vitrification process.

Intermediate level waste (ILW) consists of material that is more radioactive than LLW boundaries but that does not require heat to be removed (thermal power output is less than $2kW/m^3$). It is often in the form of irradiated material from reactors, contaminated equipment from decommissioning, chemical sludges, fuel cans etc. The concentration is > 4GBq/g of α or 12GBq/g of β/γ. Pending a suitable repository ILW is typically stored in dry, above ground facilities. Pu contaminated materials often fall into the ILW category but may have low surface doses depending on their origin.

Below this concentration the waste is classified as Low Level Waste (LLW). LLW consists typically of material from active areas such as protective clothing (e.g. gloves, tools, filters etc)

that can not be disposed of in normal waste streams and is typically sent to the Drigg Disposal Facility [4] after compaction or incineration. It requires significantly less shielding during transport and storage than ILW.

Very Low Level Waste (VLLW) may be disposed of in ordinary waste streams i.e. a landfill site. VLLW is defined such that each $0.1m^3$ of material must contain less than 0.4MBq of β/γ activity [2].

1.1.2 Nuclear Waste Characteristics

For the algorithms in question in this thesis we are mainly concerned with the assay of sealed drums of solid waste which need to be categorised into either ILW or LLW. This is performed for cost effective storage, or storage in terms of criticality or danger to humans and the environment which may occur if the waste is stored incorrectly.

The storage containers may consist of a variety of different thickness drums (mostly 205 litre steel drums) with a range of liners (HDPE or steel). The radioactive material may be contained within matrices of various compositions: paper/plastics/steel/lead and may range from milligrams to several hundred grams (to cover the operational criticality limit of 120g for fissile material) of Pu and U, possibly in close contact with low-Z elements.

1.2 Measurement Methods

Nuclear waste may be measured using either Destructive Analysis (DA) or Non-Destructive Assay. These are defined in the IAEA Safeguards Glossary [4] as:

- DA - “determination of nuclear material content and, if required, of the isotopic composition of chemical elements present in the sample. Destructive analysis normally involves destruction of the physical form of the sample.”
- NDA - “a measurement of the nuclear material content or of the element or isotopic concentration of an item without producing significant physical or chemical changes in the item.”

Destructive Analysis uses a sample of waste as a representative of a larger group; it involves transporting the sample to an appropriate laboratory for analysis, creates secondary waste and is often relatively time consuming. Although the laboratory analysis of the sample is more accurate than NDA, NDA has the benefit of measuring the whole item (for example, a drum) *in situ* in real time without disturbing the waste. It is non-intrusive and does not involve opening of the container.

For the purpose of this PhD we are concerned only with Non-Destructive Assay methods. NDA may be categorised as either passive (from spontaneous emissions of gamma-rays or neutrons) or active (from stimulated emission) analysis. Within the passive category there are a number of techniques such as calorimetry, PNCC (Passive Neutron Coincidence counting) or gamma-ray spectrometry.

X-rays may also be used to provide information on the nature of the waste e.g. using an RTR system (real-time radiography) for Non-Destructive Examination (NDE). NDE is mostly concerned with checking the waste for prohibited items and for verifying packing information or quality objectives. It can also serve to estimate the relative abundance of metals etc. This may be fed into qualitative NDA methods although on its own NDE is not regarded as assay.

1.2.1 Calorimetry

Calorimetry is the study of energy exchange between the reaction system and its environment. In terms of radiometric calorimetry this involves measuring the thermal power output for heat-producing special nuclear material (SNM), such as Pu, that are not generally be affected by the matrix or any shielding.

To measure the heat output of a Pu sample, for example, the sample would be placed into an insulated cylinder wrapped in a resistive wire inside a heat bath at constant temperature. This cylinder would be used as part of a Wheatstone bridge along with an identical control cylinder. The change in resistance can be used to give an accurate measurement of the heat output. The procedure generally takes several hours to obtain an accurate measurement and is less useful for

samples with a lower heat output, such as ^{235}U. Also it is not possible to distinguish between nuclides using this method and so it must be used with an isotopic measurement.

Calorimetry is not currently used for drummed waste due to the large time required for the waste to reach equilibrium (around 24h per item) and its poor sensitivity at the mg level, and so this method is not considered further here. This method is typically applied to bulk products, weapon components or to high (α,n) residues in small containers.

1.2.2 Passive Neutron Coincidence Counting

PNCC uses the fact that neutrons from induced or spontaneous fission are emitted in groups. $^{238,240,242}Pu$ have sufficiently large spontaneous fission neutron emission rates to allow detection, and the count rate of these correlated neutrons (for fixed isotope ratios) will be a function of the total Pu mass of the sample. The PNCC system consists of a number of ^{3}He proportional counter tubes embedded in polyethylene (the moderator) which will thermalise the neutrons so that they may be captured by the ^{3}He tubes. The captured neutrons produce a pulse train which is then analysed by a shift register able to distinguish between isolated (from (α,n) reactions) and correlated neutrons, to determine the $^{240}Pu_{eff}$ mass of the sample [5].

1.2.3 Gamma-Ray Spectrometry

Gamma-ray spectrometry uses the fact that, for a particular Special Nuclear Material (SNM) isotope the emission of gamma-rays is proportional to the mass of that isotope in the assayed sample. However the emitted radiation may not all be detected by the detector. The assay result is affected by the energy dependent full energy peak efficiency of the detector and is also impeded by the material in its path to the detector such as the measurement container, matrix and also within the source itself (self-absorption). Some of these effects may be corrected with efficiency and transmission calibrations. These are explained in more detail in Section 2.

1.3 Areas of Study

The following sections briefly outline the three areas of non-destructive analysis using gamma-rays that have been studied in this work.

Previous studies have observed an over-correction of 50% whilst measuring sources on a Canberra Segmented Gamma Scanner (SGS). These results prompted a study into the current Fleissner correction method and modelling of a range of size and shape Pu sources, which has shown it to over-correct by a factor of 1.5 at intermediate masses and under-correct at higher masses. Other methods such as the Infinite Energy Extrapolation method have also been analysed and their performance has been found to be inadequate over the range of lump sizes and shapes that may be present in a typical waste drum. The motivation behind the present study was to find a more generic approach with broader applicability [6] and an improved performance compared to the current techniques.

Correction methods such as the Fleissner and Infinite Energy Extrapolation methods require some degree of approximation and attempt to constrain the behaviour of the self-absorption to fit a simple, reproducible form. However, analysis has shown that this is not possible and so a method has been developed that involves calculating the behaviour of a large range of lump types (shapes, compounds and densities) and letting the model reveal the correlations. As a result, a new correction technique is proposed by the author in section 3 based on modelled data to correct for Pu self-absorption using the ^{239}Pu apparent masses at 129 keV and 414 keV.

Currently uranium self-absorption corrections are not applied; one possible technique to account for self-absorption involves incorporating a “lump” parameter into the estimate of the Total Measurement Uncertainty (TMU) to account for the case where all the U in a sample is concentrated into a single spherical lump (see section 5.4). The Pu self-absorption correction method developed in section 3 has been successfully adapted to be used for U (in section 4) using the ^{235}U 186 keV and ^{238}U 1001 keV lines respectively, and assuming that the enrichment is known or can be estimated.

The TMU of an assayed result encompasses all significant sources of uncertainty within the measurement and post-analysis process [7]. Current techniques provide spatial variation corrections, however these assume the photopeak may be approximated to a Gaussian distribution and only allow for the correction parameters to be inputted for one particular energy per assay. In section 5, the contribution to spatial uncertainties has been explored as a function of energy allowing for the asymmetry of the probability distribution. The method of combining uncertainties from different correction techniques for collimated and uncollimated segments has also been revisited, including the method of combination of the Pu and U self-absorption methods.

The work in section 5 has been performed as part of a project team at Canberra UK Ltd. for the SILWAS project. The contribution from the author has involved modelling of the gamma source spatial distribution and matrix effects with the Pu SAC algorithm, plus performing Pu and U measurements on the AQ2 as part of CUK Factory Acceptance Tests. Data analysis has been performed on measured results using NDA2000 and the dedicated SILWAS post analysis engines software including an early version of the developed Pu SAC and U SAC algorithms.

2 PRINCIPLES OF GAMMA RAY ASSAY

The purpose of this section is to outline the main principles of gamma-radiation, their interactions with matter and the basic concepts of gamma assay which are used throughout this report.

2.1 Gamma-Ray Emission

The emission of a gamma ray generally occurs when an excited nucleus undergoes a transition to a lower energy state of the same nuclide [8]. Their emission usually occurs after another process has occurred in the nucleus leaving it in an excited state, e.g. after β or α decay. High energy electromagnetic photons may also be produced by other processes, for example bremsstrahlung or annihilation interactions.

Gamma rays provide opportunities for detection, since unlike charged particles they cannot be deflected by electric/magnetic fields and they are much more penetrating to matter (10-100 times more penetrating that β particles [9]). The interactions of the uncharged radiation (γ rays) with matter (see Section 2.2) are used in the detection process since they transfer their energy to charged particles which are then detected via excitation and ionisation in the detector.

2.2 Interactions with Matter

2.2.1 Interaction Mechanisms

The three most important interaction mechanisms between gamma rays and matter are Compton scattering, pair production and photoelectric absorption, and all these methods result in the conversion of gamma photon energy to electron energy.

Compton scattering ([9], [10]) occurs when an incident gamma-ray photon interacts with a target electron via the electromagnetic force and consequently transfers a fraction of its energy to the recoil electron. The incident photon and the electron may be scattered through any angle and so any fraction of the gamma-ray energy may be transferred above a minimum corresponding to 180^{o} scattering. The electron is considered to be “free” although it is in fact bound to the nucleus in the outer shell.

In the presence of a nucleus, a gamma-ray photon may be converted into an electron-positron pair. This interaction is known as pair production and can only occur if the incident gamma-ray energy is at least double the electron rest mass i.e. 1.02 MeV; the excess energy is used for the kinetic energy of the created pair.

The photoelectric absorption process may occur when a gamma-ray photon is incident upon an atom and is absorbed, and a photoelectron is emitted. This emission creates a vacancy in the shell that was occupied by the electron which is filled by a transition of an electron from another shell, consequently releasing a characteristic X-ray.

2.2.2 Attenuation of Gamma-Rays

If a narrow beam of gamma radiation is incident on a detector, the radiation may be scattered or absorbed by the three interactions described above. The ratio of the number of photons that reaches the detector (I) to the number that would reach the detector without an absorber (I_o) is given by:

$$\frac{I}{I_o} = e^{-\mu.\rho.x} \qquad \textbf{Eqn. 1}$$

where μ is the mass attenuation coefficient (equal to the linear attenuation coefficient divided by ρ), ρ is the density of the absorbing material and x is the distance travelled through that material. μ is a property of an element with a γ-energy dependence and these are well documented [11], [12]. μs for compound or mixed element materials can be derived by weight fraction weighted summing.

For the purpose of the point source model used for analysis (section 3.2) and the data in Figure 6 the Genie ISOCS mass attenuation coefficient data have been used [13]. Although the original source of these data is not known for certain, it is thought to have been extracted from MCNP V.4B [14]. The data in the MCNP libraries consist of attenuation coefficient tables (separated into contributions for different interactions) versus energy at discrete energy ordinates per atomic number (element). The ISOCS program has adapted these data so that the different interaction contributions are summed and then fitted to polynomials rather than using table interpolation

within ISOCS. If there is a K-edge in the energy range then multiple polynomials are used. ISOCS uses total minus coherent scattering mass attenuation coefficients since for many geometries, in and out scattering without energy loss cancels so that coherent scattering may be ignored.

One of the 'best' (current and comprehensive) sources of mass attenuation coefficient data is the NIST XCOM database [15]. This database may be used to calculate photon cross-sections and total attenuation coefficients, plus individual coherent and incoherent scattering, photoelectric absorption and pair production cross-sections for any element compound or mixture within the energy range 1 keV to 100 GeV.

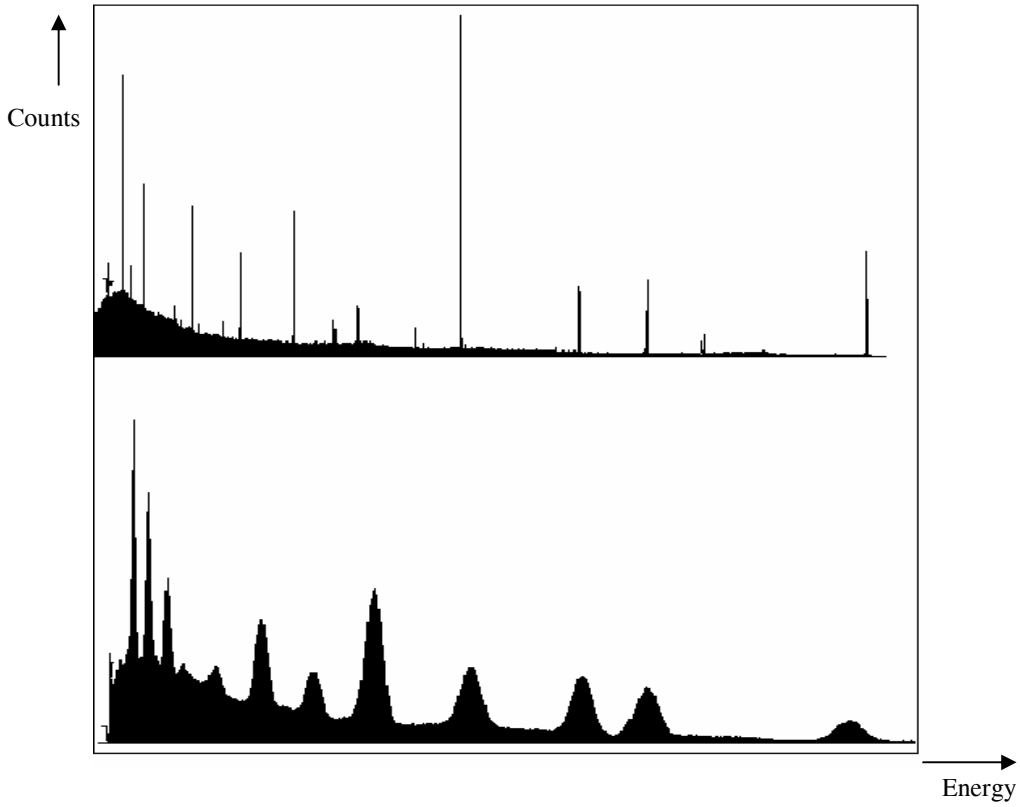

Figure 1: Example of γ specta from NaI(Tl) (bottom) and Ge detectors (top) showing the higher resolution of the Ge detector compared to NaI(Tl) for a similar energy range [16].

2.3 Gamma Spectra

The two main types of detectors used for gamma radiation detection in waste assay are the Ge semi-conductors and NaI(Tl) scintillator detectors. The NaI(Tl) detector has a higher detection efficiency but the Ge detector has a much better energy resolution (allowing a nuclide identification to be performed for complex waste spectra) and so compensates to have a comparable detection limit.

Figure 1 and Figure 2 show examples of Ge and NaI(Tl) spectra. As shown, the individual peaks of the Ge spectrum may be easily resolved in this example.

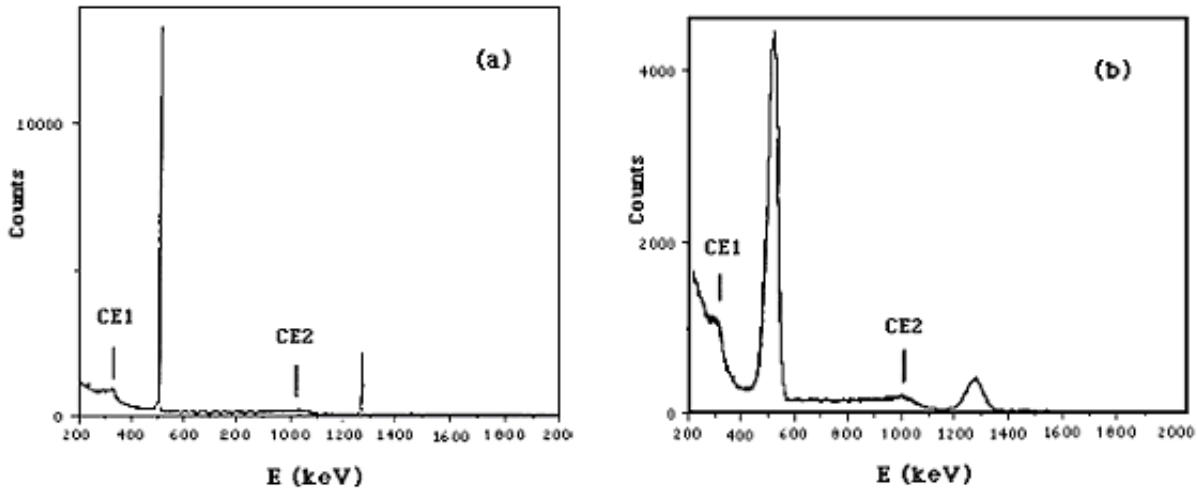

Figure 2: Gamma ray spectra of ^{22}Na using (a) a Ge(Li) and (b) a NaI(Tl) detector [17].

Figure 2 compares the spectra over the same energy range for a ^{22}Na source. The ^{22}Na peak is seen at 1275 keV and also because ^{22}Na is a β^+ emitter annihilation radiation is observed at 511 keV. Additionally two other features are labelled as CE1 and CE2 - the Compton edges. The CE2 points where a 1275 keV gamma ray enters the detectors, interacts via Compton scattering with an electron such that its direction is completely reversed and then leaves the detector without further interaction. The region before CE2 is its Compton "plateau" which results from other (non-backscatter) Compton interactions where the reduced energy photon escapes the detector. CE1 is the corresponding Compton edge for the 511 keV peak.

2.4 Spectral Analysis

2.4.1 Calibrations

To obtain qualitative data, such as nuclide identity and activity measurement, from gamma-ray spectra a number of stages must first be performed such as an energy calibration and efficiency calibration. In addition, if the system has a transmission gauge (used to derive a matrix attenuation correction factor), a transmission calibration is required. These serve to provide the analysis software with information about the system's setup and overall behaviour.

The energy calibration (performed with known sources) determines the energy-to-channel relationship. The final positions of the peaks within the spectrum are defined using the amplifier gain (to determine the distance between peaks) and the ADC zero (the zero offset to set the exact peak positions). Modern energy calibration software will also calibrate the resolution (FWHM) and energy tail of the peaks.

The efficiency is required to interpret count rates for a given measurement geometry into bequerels. This is dependent on the geometry of the detector i.e. the detector-sample distance, spatial distribution, sample density and intrinsic detector efficiency. The absolute efficiency [18] is defined as:

$$\text{Absolute efficiency} = \frac{\text{Counts per sec observed in the detector}}{\text{Gammas per sec emitted by the source}} \qquad \textbf{Eqn. 2}$$

An efficiency measurement is performed with a known multi-line source and the efficiency as a function of energy is calculated as:

$$eff(E) = \frac{A_P(E)}{t \times Act \times Abundance \times D} \qquad \textbf{Eqn. 3}$$

where A_p is the net peak area, t is the live time (secs), Act is the activity in Bq of the source at the calibration certificate time and D is a factor to decay correct the activity to that at the acquisition start time:

$$D = e^{-\frac{\ln(2) \times t_w}{T_{1/2}}} \qquad \textbf{Eqn. 4}$$

where t_w is the decay time of the calibration source and $T_{1/2}$ is the half life of the calibration nuclide [19].

Since only a few energies (e.g. for ^{152}Eu, 14 lines) are available within the calibration source interpolation is used for the curve to determine the efficiency in between these energies.

If the detector system has an active gamma-ray transmission facility then a transmission calibration will be performed, which is dependent on energy and geometry. For this a reference measurement of the count rate collected by the detector with the transmission source exposed for an empty container is required. Since only the lines of the transmission source will be found in the spectrum a transmission curve must be interpolated, as for the efficiency calibration.

During the main assay the transmission calibration is compared to the transmission measurement to determine the average density of the matrix inside the container, assuming the matrix is homogenous [8]. One problem that can occur is if the transmission beam passes through a solid lump of material, for example Pu. In this case the software would assume that the average density of the drum matrix is much higher than is the case.

2.4.2 Assay Analysis Software Stages

Once the calibrations have been performed and the system has been set up correctly, a transmission measurement (if required) and a passive assay are performed. At this stage generally software is invoked to perform the spectral analysis. This may consist of a large number of stages. The main stages that may be used are listed below:

- Peak analysis - the peaks are first detected above the background by the software and their energies and peak areas are determined.
- Nuclide Identification (NID) - The peaks are identified against nuclides and isotopes defined in a nuclide library based upon energies etc. A number of line energies may be checked to determine if an isotope is really within the assayed container.
- Efficiency correction - The true activity of the line is calculated based upon the efficiency curve calculated by the efficiency calibration performed previously and the equation stated in section 2.4.1 [20].

- Transmission correction (if required) - The expected matrix attenuation factor is calculated from the transmission ratios in the (active) transmission CAM files and used to calculate a corrected efficiency that would give the true activity in the segment on the assumption of uniform matrix density and uniform distribution of activity.
- Other corrections - other corrections may then be performed for self-absorption within Pu in the container for example.
- TMU and MDA analysis [21] - the Total Measurement Uncertainty (TMU) of a nuclide/isotope is quoted if the nuclide has been identified by NID. This uncertainty aims to encompass all the possible uncertainties that could have affected the measurement e.g. spatial, lump, statistical, systematic uncertainties etc. The Minimum Detectable Activity (MDA) (or a Less-Than Level) is quoted when a nuclide has not been identified by NID; it is the minimum activity that must be present to be sure an isotope is present. The value is then quoted as less than (<) this value.

2.5 The AQ2 - An Example of a Waste Assay System

An example of a gamma waste assay system is Canberra's AQ2 ([22], [23]), as shown in Figure 3. The AQ2 consists of a shielded chamber within which a drum is rotated (to average out heterogeneity) and assayed using three fixed Broad Energy Germanium detectors (BEGe), visible on the right hand side of the inner chamber wall. The BEGe detectors are sensitive to gamma rays in the energy range 3keV to 3MeV.

Figure 3: Canberra's AQ2 gamma scanner used as part of the SILWAS to measure the AE4043/nn sources.

An AQ2 has been used to perform simulated waste measurements in sections of this thesis as part of the Solid Intermediate Level Waste Assay System (SILWAS) (see Figure 4). The SILWAS was designed to measure the fissile content of solid waste drums and hence sentence them as LLW or ILW, using two components: an Auto Q2 (AQ2) and a High-Efficiency Neutron Counter (HENC) ([24], [25]) both operating with Canberra's NDA2000. The two systems work complimentarily, controlled by a 'Master control' PC with external analysis and decision making software (see

following sections) to decide which instrument offers the best result based upon effects of substances present in the waste drums (attenuation, multiplication etc), and to give activities of selected nuclides, hence sentencing the drum.

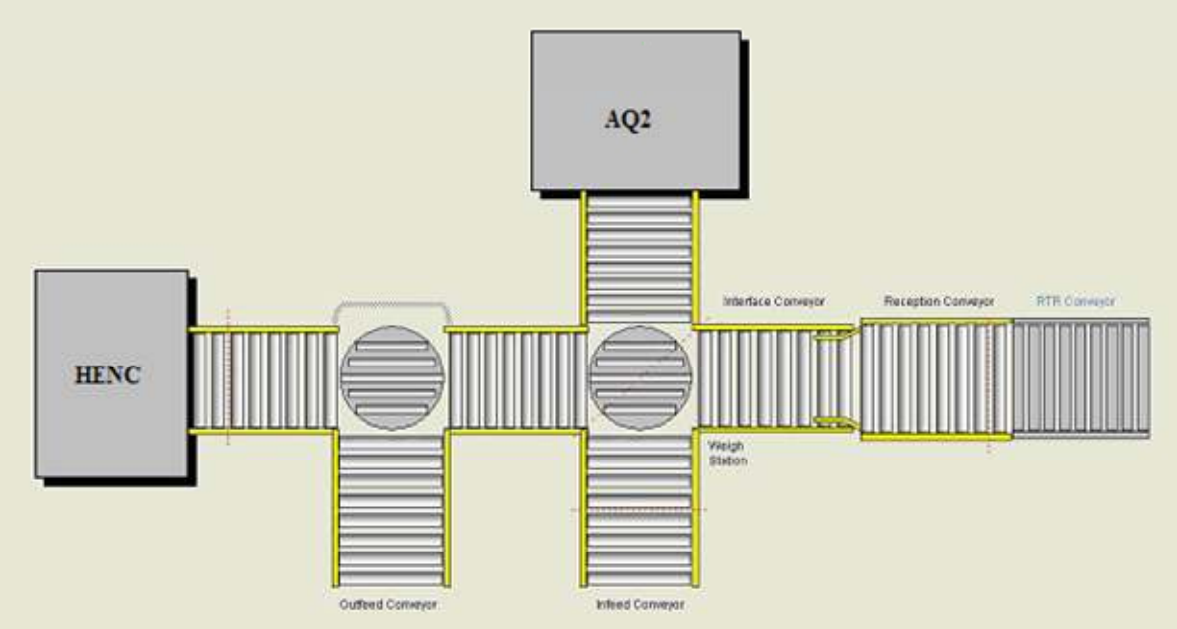

Figure 4: A plan view of the SILWAS system showing the AQ2 and HENC chambers with connecting conveyors and turntables.

The shield of the AQ2 is constructed from 10cm-thick low-background steel. The steel and other materials used to construct the instrument are chosen so as to minimise the naturally occurring γ emitters that could be present.

Three BEGe 2820 detectors [26] are used to minimise spatial source distribution effects and to increase sensitivity. (The individual detector results are also referred to as segment results). Three ^{152}Eu transmission sources (approximately 370 MBq each, emitting at 122 keV, 244 keV, 344 keV, 779 keV, 964 keV, 1112 keV and 1408 keV) are mounted in a shielded container on the outside of the chamber opposite the three detectors to determine the mean density of the matrix at

the three heights through attenuation. Mechanically-operated shutters are operated by the system to expose and shield the transmission sources inside the chamber.

Inside the shield, the drum is placed onto a rotating platform to minimise the effects of source and matrix non-uniformity. This rotation is used with the Dual Multi-Spectrum Scaling (DMSS) allowing spectra to be obtained for eight rotation sections. The use of this method known as NUDS is discussed in section 2.5.1.2.

This AQ2 has been calibrated for the 6 main drum types listed below with their SILWAS drum types and a brief description of the contents:

- IND10164 – 205 litre drum with no internal furniture other than a PVC bag and fibreboard liners
- AWG565 – a 205 litre drum with a 5 mm HDPE push-lid liner
- AWG588 – a 205 litre drum with a 7 mm HDPE screw-lid liner
- ASC047 Option 2 – a 210 litre drum with no liner and with a 100 litre drum in the centre
- ASC047 Option 3 – similar to an Option 2 but with a 1.5 mm steel inner liner
- ASC047 Option 4 – similar to an Option 2 but with a 2.5 mm steel inner liner

2.5.1 Analysis Stages

The analysis of results for SILWAS is performed in several different stages:

- The AQ2 performs a brief 100s assay of the drum and performs a drum type calculation based upon the transmission of the top transmission source (which does not pass through the matrix)
- The determined drum type is used as the basis for the efficiency and transmission calibrations for the main (120s active and 300s passive) measurement. NDA 2000 performs the measurements and basis spectral analysis e.g. NID, matrix attenuation correction, isotopic determination, etc.
- The drum is conveyed to the HENC to perform the neutron assay measurement using NDA2000, followed by basic neutron analysis.
- A set of Post Analysis engines are used to perform additional analyses including Pu and U lump correction, NUDS analysis, isotopics combination, TMU and MDA calculations, light

element neutron multiplication analysis, Pu combination decision making, α and β activity tables and LLW/ILW sentencing. These are described in the next section.

A custom report generator is then called to report the data in the specified user format. Selected post analysis engines are outlined in the sections below.

2.5.1.1 Lump corrections

The Post Analysis engines perform self-absorption corrections for Pu and U on an instrument basis i.e. summing the individual detector results before performing the correction. The methods for these corrections are described in detail in sections 3 and 4. However, since the SILWAS was installed whilst the SAC methodology was in its early stages of development, the first generation (6^{th} order log polynomial) method has been used for the curve fits (see section 3.8.2). The selected isotopics are used to convert the total Pu mass results for each of the Pu isotopes.

If the U self-absorption correction cannot be performed due to one of the lines not being identified for example, a U lump component is incorporated into the TMU.

2.5.1.2 Non-Uniformity Detection Software (NUDS)

The non-uniformity detection software (NUDS) has been designed by Canberra to identify any non-uniform matrix density and source distribution [27]. A Dual Multi-Spectrum Scaling (DMSS) is used to obtain eight separate spectra for the eight rotation sections while the drum rotates during the measurement.

The passive counts for each octant for the 186 keV line for ^{235}U, 1001 keV line for ^{238}U and 414 keV line for ^{239}Pu, plus the nearest transmission line for each octant for each for these lines are stored. The program then calculates the longitudinal and vertical, matrix and source NUDS values and errors for each of the three isotopes. The results are presented graphically in the report (see Figure 56 as an example).

The source longitudinal value for the ^{235}U record is also used and compared to a 'lump threshold' set by the user to determine if the sample may be considered to be uniform or not i.e. if the value is greater than the lump threshold set by the user the sample is said to be non-uniform and the user specified minimum number of lumps is used as the number of U spheres (when the U self-absorption correction has not been performed - see section 2.5.1.1).

2.5.1.3 MDAs and TMUs

The MDA engine reads NDA 2000 calculated MDA values for those nuclides that are not detected for each segment and applies a correction for matrix attenuation and for spatial variations (see section 5.5 and 5.2). If ^{239}Pu is an MDA then the other Pu isotope records are found and have their MDAs scaled according to the current isotopics. A similar method is performed if both ^{235}U and ^{238}U are MDAs. This is performed before the attenuation and spatial MDA corrections so that all MDAs on the report are corrected accordingly.

The TMUs (see section 5) are made up from the following sources:

- NDA 2000 NID uncertainties which include counting statistics in the assay data, detection efficiency calibrations, transmission calibrations, nuclear data in the nuclide library etc
- Source spatial variations
- Lump TMU contribution for ^{235}U

The gamma-ray used to determine the ^{235}U result is 186 keV which is highly attenuated in uranium metal. In view of the likelihood that the uranium may be present in the waste in the form of metal pieces, a 'worst-case' contribution to the positive TMU for ^{235}U is calculated. This is based on the assumptions that the U will be present in a number of equi-sized spheres with density 18.7 g/ml and that the number of spheres will be either a minimum or maximum (user set) number of lumps according to whether the longitudinal non-uniformity parameter for passive ^{235}U calculated in the NUDS engine exceeds the *LumpThreshold* value.

If USAC has not been performed then a ^{235}U lump uncertainty is additionally combined. This lump uncertainty is calculated and combined with the other sources of error on a segment basis.

2.5.1.4 Light Element Multiplication

The Light Element Multiplication engine looks for ^{22}Na (indicating fluorine in intimate contact with α-emitting material) and ^{9}Be in the spectrum and compares the activities/count rates to threshold values set by the user to determine if any light element multiplication has taken place, e.g. in the interaction:

$$^{19}\mathrm{F} + {}^{4}\alpha \rightarrow {}^{22}\mathrm{Na} + {}^{1}\mathrm{n}$$

If the activity is greater than the limit set by the user then the a flag is set, otherwise it is assumed that there is no ^{19}F(α,n) reaction taking place.

2.5.1.5 Source of Result Decisions and ILW/LLW Sentencing

A complex decision tree has been devised to determine which instrument offers the best source of Pu result based upon the calculated mass and uncertainty or MDA, plus other factors such as evidence of light element multiplication and the HENC reals to totals ratio. This process will not be described in detail in this report but more information may be found in Canberra documentation [28]. The chosen source of result is combined with the other data and user-specified limits to determine:

- If the combined Pu and ^{235}U mass is below the allowed fissile mass limit (~120g)
- If the total alpha activity $\frac{Total\alpha + k\sigma_{\alpha}}{grossweight}$ is less than the UK LLW alpha limit of 4 kBq/g
- If the total beta activity $\frac{Total\beta + k\sigma_{\alpha}}{grossweight}$ is less than the UK LLW beta limit is 12 kBq/g.

where k is a user-specified confidence factor.

2.5.2 Calibration

2.5.2.1 AQ2 Energy and Transmission Calibrations

The energy and FWHM calibration of the γ-ray spectrum has been performed using the normal Genie 2000 method, as described in the Genie 2000 Operations Manual [29]. The spectrum gain may be set by collecting a spectrum from a multi-line gamma source in front of the detector using Genie 2000 'Gamma Acquisition and Analysis' (GAA). For this purpose the ^{152}Eu transmission source is used by exposing the source using the transmission shutters. The coarse and fine gains are adjusted until the 1408 keV ^{152}Eu line is placed at channel 15000 to give as much spread between peaks without going off the channel limit. The conversion of channel number to energy i.e. the calibration of the spectra can be performed by selecting *Calibrate*| *Energy Full*| *By Certificate File* and choosing the appropriate certificate file for the source.

The system also requires transmission calibrations for each container and geometry type. Transmission Calibrations are performed in the standard manner, as described in the NDA 2000 User's Manual [30]. The process involves placing an empty drum in the AQ2 and performing a Transmission Count on the AQ2 PC specifying the drum type in the information set-up screen. The NDA 2000 Calibrations program is then opened and the relevant counter type, calibration type, geometry and container type are selected. The method is followed as described in the NDA 2000 User's Manual [30].

2.5.2.2 AQ2 Efficiency Calibration

The SILWAS was intended to assay two different sizes of drums, 205 litre and 210 litre, each of which have 3 variations of internal furniture, giving a total of 6 main physical drum types (as described in section 2.5). Efficiency calibrations are required - two for each container type to account for the cases with and without the sliding filters (1.5mm thick sheets of tin to reduce the countrate for very active drums). Thus 12 efficiency calibrations are required in total.

The effects of γ-ray absorption in the internal furniture and the walls of the drums are incorporated in the efficiency calibration for each drum type. The effect of γ-ray absorption in the waste material inside the drum (matrix), which can vary from drum to drum, is handled by using the

gamma transmission measurement (see section 5.5). The matrix analysis makes the assumption that the matrix attenuation is uniform at least throughout each detector segment.

In practise it proves difficult to measure the VWA efficiency because of the difficulties in accurately simulating a VWA γ-ray source throughout the internal volume of the drum. Consequently the efficiencies have been derived by numerical integration of contributions to the detector count rate from individual voxels with a computer model (NDA Model [31]).

Spectra have been acquired for a calibrated multi-line near-point disc source on the rotation axis of the turntable at the same height and known distances from the detectors, to provide absolute peak efficiency data for the model. The source was placed inside a drum to support the source only. The attenuation in the drum wall is factored out in the subsequent calculations and replaced with the calculated drum wall attenuation for the container being modelled.

A Certificate File is created for the multi-line source, containing the number of gamma-rays emitted per second by the source for each line calculated at a single date and time (obtained from the source's calibration certificate). Using this Certificate file and the measured spectrum file an efficiency calibration is generated using GAA. The NDA model can then use the point-source efficiency data in this file to calculate the probability that photons that strike the detectors will produce a peak event.

The NDA Model produces VWA efficiencies for a range of energies selected to span the spectral range of interest i.e. 60 keV to 1500 keV. These efficiency triplets (energy, efficiency and uncertainty) are then entered into an NDA 2000 Calibration which is a set of files maintained by NDA2000.

Five of the six container-type efficiencies could not be created by direct measurement because gamma sources were not available to reproduce accurately a uniformly distributed activity. For this case, rod sources were used that are the correct length for 205 litre drums with no internal furniture. The VWA efficiency for the IND10164 container has therefore been separately

measured purely as a supporting check on the validity of the method used for the computed efficiencies.

The rod sources are a set of 7 calibrated multi-line sources that are placed within the drum in a jig to simulate a uniform spatial distribution of activity for the rotating drum. These sources are 830mm long (with a 2mm end cap at each end giving an active length of 826mm) thin aluminium tubes filled with epoxy that has been doped with known amounts of selected gamma-ray emitting isotopes. Table 1 lists the isotopes and their activities.

Table 1: Activities of isotopes in CUK Rod Sources used for the AQ2 Efficiency Calibration.

Line	Source	10035	10036	10037	10038	10039	10041	10042	Total
Isotope	Half-life (years)	kBq	kBq	kBq	kBq	kBq	kBq	kBq	kBq
Am-241	432.7	830.8	798	849.4	826.2	827.4	827.9	820.6	5780.3
Ba-133	10.54	450.7	432.9	460.8	448.2	448.9	449.2	445.2	3135.9
Eu-152	13.33	458.5	440.5	468.8	456.1	456.7	457	452.9	3190.5
Cs-137	30.17	92.07	88.44	94.13	91.57	91.69	91.75	90.94	640.59
		Strengths quoted are 1200hrs PDT July1 2001 in kBq							

Figure 5 shows a plot of the VWA efficiency computed for the IND10164 Container type for each of the 3 detectors and the directly measured efficiencies obtained using the rod sources. The Detector 2 curves lie on top of each other fairly well and consistently with the error bars. These errors are dominated by the contribution from the absolute uncertainty on the activities of the sources in the certificate files.

Detectors 1 and 3 show small systematic differences between the measured and computed which can be attributed to difficulties in reproducing a truly VWA source distribution with rod sources. The problem is more apparent at the ends of the sources where the real drum and line source dimensions do not exactly match the model ideals.

The comparison provides confidence that the computed efficiencies are consistent with real measurements and justifies the use of computed values, which are found to be universally more reliable and consistent than measured ones.

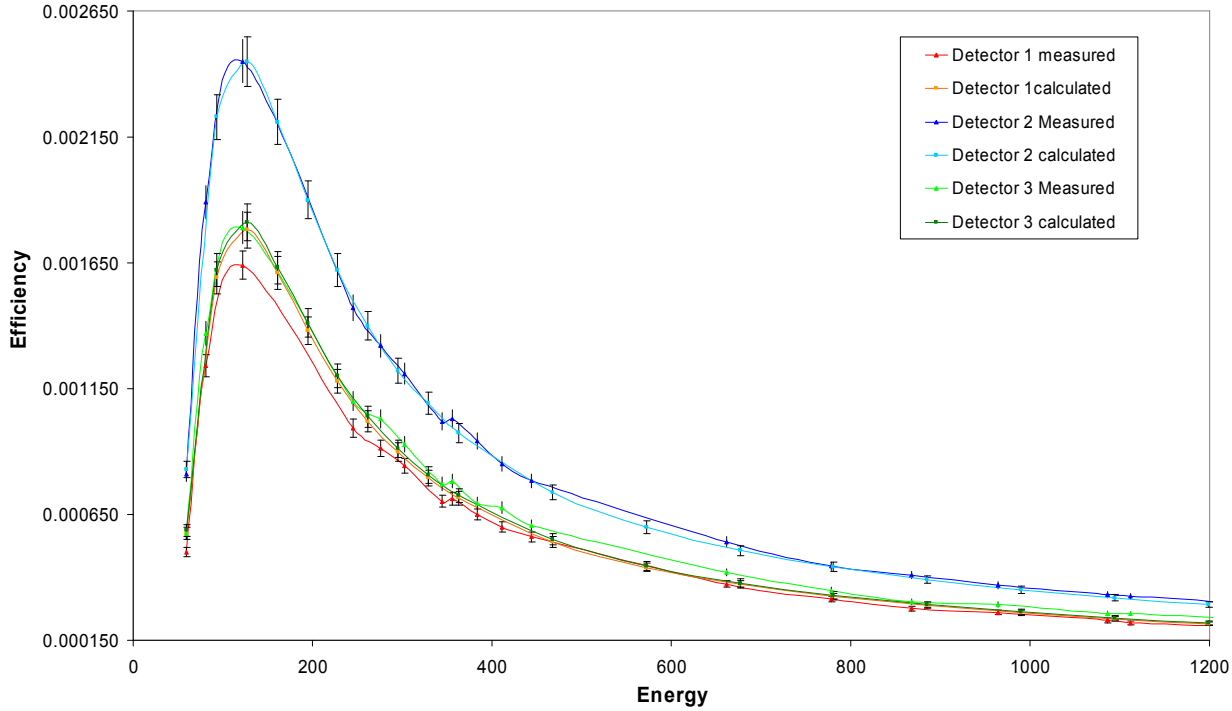

Figure 5: Plot comparing computed VWA peak efficiencies for the IND10164 drum type with a measurement of the same drum type using 7 calibrated rod sources.

2.5.2.3 HENC Calibration

The calibration of the HENC includes an add-a-source calibration, neutron multiplicity characterisation and Pu mass calibration. These calibration methods will not be detailed in this thesis, however more information may be found in Canberra documentation ([32], [33]).

3 PLUTONIUM SELF ABSORPTION

3.1 Introduction

During previous work an issue with the current plutonium self-absorption correction was highlighted; for an AE 4043/5 Pu sample [31], a consistent over-correction of 50% was observed when measuring with an SGS (Segmented Gamma Scanner). The possibility of inaccurate measured line intensities as the source of the problem was ruled-out by comparing uncorrected 129keV and 414keV assay results with calculated SAC (self absorption corrected) emission rates for this sample. This prompted detailed analysis of the Pu self-absorption behaviour for various lump shapes and materials (densities) and hence the search for a more accurate SAC method. One resolution to this problem is to calculate self-absorption factors using analytical methods [35]. Due to the extreme non-linearity in the nature of gamma attenuation these methods generally require some degree of approximation.

The bias caused by self-absorption in lumps is long known [36], though advances failed to develop until the early 1980s when computer processing became more widely available. In 1981, work concentrating on the analysis of HTGR fuel resulted in a correction algorithm assuming single-sized lumps in heterogeneous materials [37]. This assumption was also used for LANL SGS and TGS correction techniques, using a least squares weighting algorithm ([38], [39]). This work has been extended for a mixture of lumps, separated into two main portions which are treated separately [40]. Recent work by Croft et al. [41] has developed and examined calculation tools for analysing the self-absorption within specific shapes in the far-field approximation.

This chapter initially examines the problem of self-absorption within lumps of Pu using current SAC techniques, concentrating on the Fleissner method [42] as a standard correction technique (available as a module in Canberra's NDA2000 suite). Data were modelled for Pu lumps of various sizes and shapes in the near-field, using a numerical approach, reducing any assumptions about the sample and its distribution. A new SAC algorithm is then proposed and tested using modelled data for three different lump types.

The new technique is then tested using measured data from encapsulated AE4043/nn PuO_2 samples, following an investigation into the sources themselves and an estimation of their average density based upon observations from measurements.

The results from both the measured and modelled data are examined. There is also a brief study to investigate the use of the new SAC algorithm with multiple lumps present.

3.1.1 Why is Pu a Problem?

The measurement of Pu poses a problem in each of the three measurement techniques described in Section 1.3. Both calorimetry and PNCC measurements require the isotopic composition of the sample to be known. This is not always the case for waste and so a further measurement, using a HPGe detector, for example, is generally required. Also for the PNCC, multiplication may occur if light elements are in close contact with the Pu. Pu in compact form is self multiplying and if the (α,n) yield is also high (e.g. ^{241}Am-rich and if low-Z materials are present) the induced fission component can be significant. Similarly if the Pu is in intimate contact with materials that can also be fissioned or multiply fast neutrons (n,2n). In parallel, γ-ray assay suffers from attenuation within the Pu itself.

Although ^{239}Pu emits many lines, for γ -ray assay Pu is generally measured using ^{239}Pu lines at around 400 keV e.g. 375 keV and 414 keV since these are least affected by matrix attenuation and lump effects. These lines exhibit the best detector properties of good penetration in waste and lumps and show a reasonably high intensity. The assay of plutonium in waste is complicated by the physical form in which it may occur, such as particles or even large lumps which may exhibit a high degree of self-attenuation effects due to the mass attenuation coefficients at the assay energy.

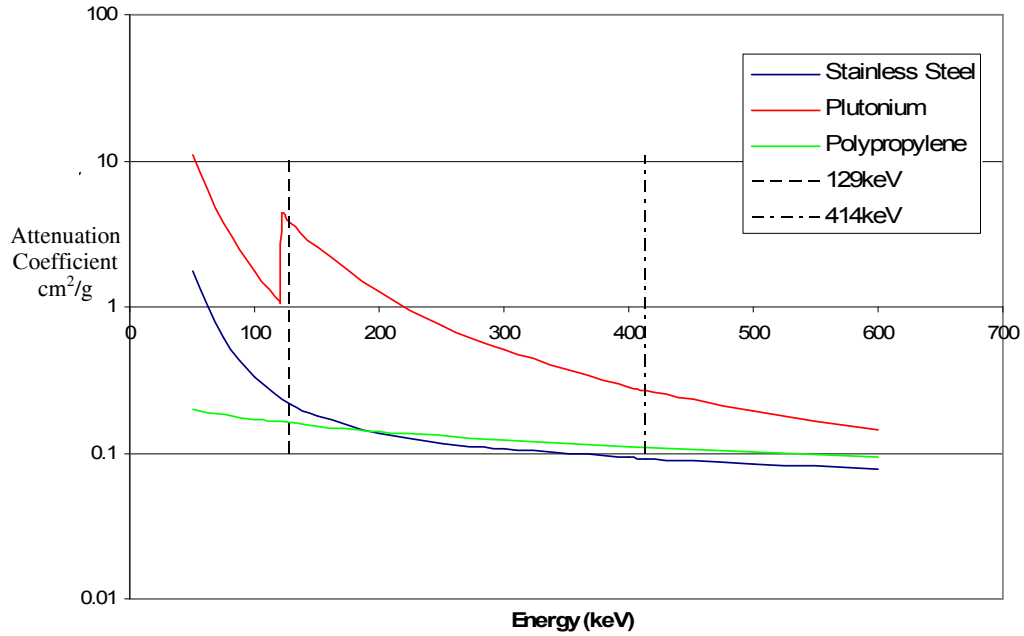

Figure 6: μ vs Energy for various materials generated from Genie ISOCS attenuation coefficient data (mu04_8lb.txt file).

Figure 6 shows the mass attenuation coefficient (μ) versus energy (E) for three different materials: stainless steel, polypropylene and plutonium, and the location of the 414 keV line is indicated. Also shown is the location of the strong 129 keV line from ^{239}Pu. The ratio of the mass attenuation coefficients for the two energies (129 keV and 414 keV) for polypropylene and stainless steel is much less than that for Pu. Also the 129 keV energy line lies just above the K-edge of the Pu curve (121.8 keV), hence Pu suffers much more strongly from attenuation effects at these energies. Consequently the 129 keV and 414 keV pair offers a better differential absorption in this set of more prominent γ-ray spectra lines. Those properties of the 129 keV and 414 keV lines form the basis of methods for correction for self-absorption in Pu.

3.1.2 The Fleissner Method

A standard SAC algorithm offered in Canberra's NDA2000 data acquisition and analysis suite [43] was developed empirically by John Fleissner [42] for the assay of canned radioactive waste containing a distribution of lump sizes: The approach involved comparing gamma-assay results

against calorimetric-based assays of the same item and fitting mass as a function of energy. The form of the correction using just two lines is shown below:

$$M_i = M^o e^{-\frac{\beta}{E_i}} \qquad \text{Eqn. 5}$$

where M_i and E_i are the apparent intensity and energy of the i'th line respectively, M^o is the corrected activity of the nuclide and β is a model parameter. This correction can be derived from first principles under the assumptions that the self-absorption is not severe and therefore the method may be less appropriate for single lumps and encapsulated sources. This basic model assumes that all of the nuclide experiences self-absorption. If some of the material does not experience self-absorption then multiple energy lines may be used in the equation below:

$$M_i = M^o \left(1 + \alpha \left(e^{-\frac{\beta}{E_i}} - 1 \right) \right) \qquad \textbf{Eqn. 6}$$

where α is the ratio of the self-absorbed activity to the corrected activity and is constrained to be ≤ 1. The equation may also be expressed as:

$$M_i = \left\{ M^0 (1-\alpha) \right\} + \left\{ M^0 \alpha e^{-\frac{\beta}{E_i}} \right\} \qquad \textbf{Eqn. 7}$$

where the first component of the apparent mass that is due to zero self-absorbing material (i.e. the matrix), and the second component is the fraction of apparent mass that is due to the self-absorbing material itself. Therefore if α is zero then the apparent masses have suffered no self-absorption; and if α is unity then the apparent masses are due to self-absorption within the lump only, and the equation simplifies to the two-line method (see above).

The Fleissner SAC methods are made available with NDA2000 with the onus being on the user to validate its suitability for the particular waste form; the Molten Salt Extract residue for which the approach was initially developed may not be a good match for another person's needs.

The basic two-line and the three-line methods have been analysed using a point source model which is described in Section 3.2. Another possible route for study that has not been considered in this PhD is to investigate the extension of the Fleissner equations to cases of E_n.

3.1.3 The Infinite Energy Extrapolation Method

The infinite energy extrapolation method [44] determines an estimate of the self-absorption corrected mass based upon a curve of the apparent mass (m_i) versus the reciprocal of the energy ($1/E_i$), for example, for a series of lines (i) from the same isotope. For example, for a 28g PuO_2 (24.7g Pu) stainless steel encapsulated source (see section 3.3) in an empty 200 litre drum, measured for 300s using an AQ2 as described in section 2.5, the measured ^{239}Pu lines are 129 keV, 203 keV, 345 keV, 375 keV, 392 keV, 414 keV and 451 keV. A graph of the apparent mass versus 1/E is shown in Figure 7.

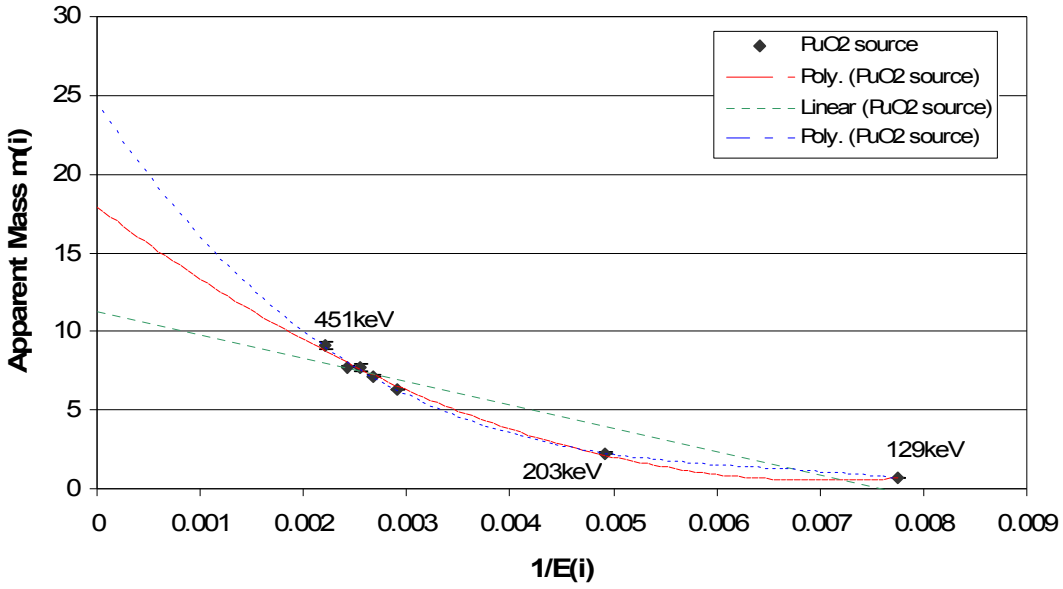

Figure 7: Graph showing the apparent ^{239}Pu mass m_i (g) and uncertainties against $1/E_i$ for AE4043/10 in an empty 200 litre drum showing a linear, 2nd (green) and 3rd (blue) order polynomial curve fits.

The extrapolation intercept of the curve will give an estimate of the ^{239}Pu mass of the sample. The graph shows three types of curve fits to the data: linear, 2nd and 3rd order polynomial fits. The 3rd order polynomial fits this set of data the best with an R^2 of 0.997 (R^2=0.994 for 2nd order polynomial and 0.908 for the linear fit). This fit estimates a Pu result of approximately 32.3 g, an

overestimation compared to the true Pu mass of 24.7 g. The 2nd order polynomial fit gives a good estimation of 23.6g, whereas the linear fit underestimates the mass as 14.7 g.

Another possibility is to plot the natural logarithm of the apparent mass versus 1/E. This method is linked to the 2-line Fleissner method since the Fleissner equation (see section 3.1.2) may be rearranged into the form:

$$\ln(M_i) = -\frac{\beta}{E_i} + \ln(M^o) \qquad \textbf{Eqn. 8}$$

where the y-axis may be given by $ln(M_i)$ and the x-axis as $1/E_i$, with the y-intercept as $ln(M^o)$ and negative gradient of the graph as β.

These methods are compared to the three line Fleissner techniques and the new Pu SAC method in section 3.12.

3.2 Description of the Point Source Model

To perform the calculations for the analysis of the basic Fleissner method and other self-absorption modelling a point source model developed by M. Wormald [31] has been used. It is based upon the physical principles, requires only the photopeak energies (since it is based upon a germanium detector set-up) and assumes only knowledge of nuclear data.

The model allows a lump size, shape (cylinder or cuboidal shapes) and composition to be specified by the user. The model breaks the lump up into a specified number of voxels (volume elements - see section 3.6), defined by radial, polar and height integration intervals for cylindrical lumps, and lateral, depth, height and rotation integration intervals for cuboidal lumps.

The model sets the gamma-ray production in each voxel as the volume of the voxel and computes the probability of the gamma-rays reaching the detector without scattering or absorption. The voxel contributions are integrated over the whole lump and the calculation repeated with the density in the attenuation function set to zero, the ratio of these results defines the self-attenuation factor (SAF) for that gamma-ray line energy (i), i.e.

$$SAF_i = \frac{R_{0i}}{R_{si}} \qquad \textbf{Eqn. 9}$$

where R_{si} is the detected count rate from the sample and R_{0i} is the detection rate there would be with no self absorption in the sample for the energy i. The apparent masses may then be calculated using:

$$M_i = SAF_i . M_T \qquad \textbf{Eqn. 10}$$

where M_i is the apparent mass at the line energy i, SAF_i is the self attenuation factor at energy i, and M_T is the true mass of the modelled sample.

The incoherently scattered component of the gamma-ray flux reaching the detector can safely be ignored where high resolution Ge detectors are to be used in the measurement since the scattered photons are almost invariably energy-degraded to the continuum below the photo-peak. The coherent scattered component (which does not involve energy loss) may be neglected since it is assumed that the flux in and out of the geometry will cancel.

3.3 AE4043/nn Sources

In order to better validate the point source model the modelled sources should be compared to experimentally-measured sources. Since bare sources are not available for safety purposes the model was tested with stainless steel encapsulated sources. In order to correctly model the sources themselves they must first be examined and their structure understood in detail. In this section we compare the fabrication details of the sources with empirical validation measurements to reveal some subtle differences. These differences are important when using the sources to test any Pu SAC algorithm.

Table 2: Isotopics for AE4043/nn sources, measured 27 January 1990 [45] and calculated 20 January 2007.

	Measured 27/01/90		Calculated 20/01/07	
Isotope	Weight %	Uncertainty %	Weight %	Uncertainty %
Pu-238	0.121	0.001	0.107	0.001
Pu-239	76.792	0.022	76.702	0.022
Pu-240	21.336	0.019	21.564	0.019
Pu-241	2.052	0.002	0.917	0.010
Pu-242	0.701	0.002	0.710	0.002
Am-241 (with respect to Pu)	817 ppm	2 ppm	12228 ppm	103 ppm

The sources which have been used to test the Pu SAC algorithm experimentally are the AE4043/nn sources. These are stainless steel (double) encapsulated PuO_2 sources containing the relative isotopic composition in Table 2. Although the outer structure of the sources is documented thoroughly ([45], [46]), the internal composition (PuO_2 density, fill height, symmetry etc.) is not well known.

The sources consist of a series of 1.3mm thick stainless steel capsules, shown separately in Figure 8 and Figure 9. Figure 8 shows the components of the stainless steel encapsulated sources, including the tools for extracting the inner piston and compressing the PuO_2.

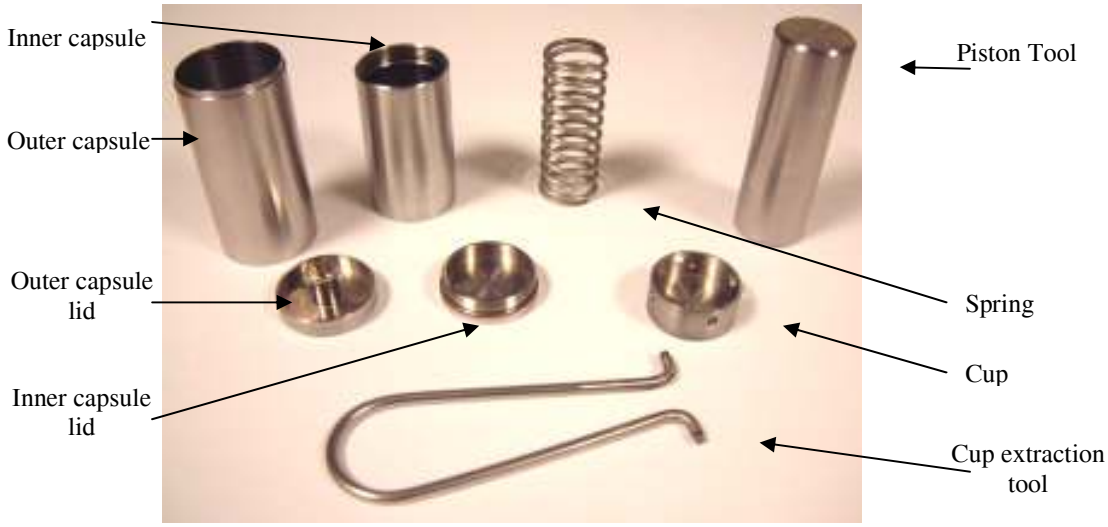

Figure 8: The AE4043/nn source components including the inner and outer capsule and lids, cup, spring, piston tool and cup extraction tool (excluding the spring locators).

Figure 9: The AE4043/nn source component configuration minus the spring locators.

The source components are configured as shown in the photograph in Figure 9 and the internal sketch in Figure 10. The PuO_2 is compressed into the base of the inner capsule using the piston tool and the cup. This is then held in place firmly by the spring and locators, which is secured between the cup and the inner capsule lid. The inner capsule is then fitted into the outer capsule and sealed. The spring was not fitted for sources containing greater than 28 g of PuO_2 (items AE4043/9 and /10).

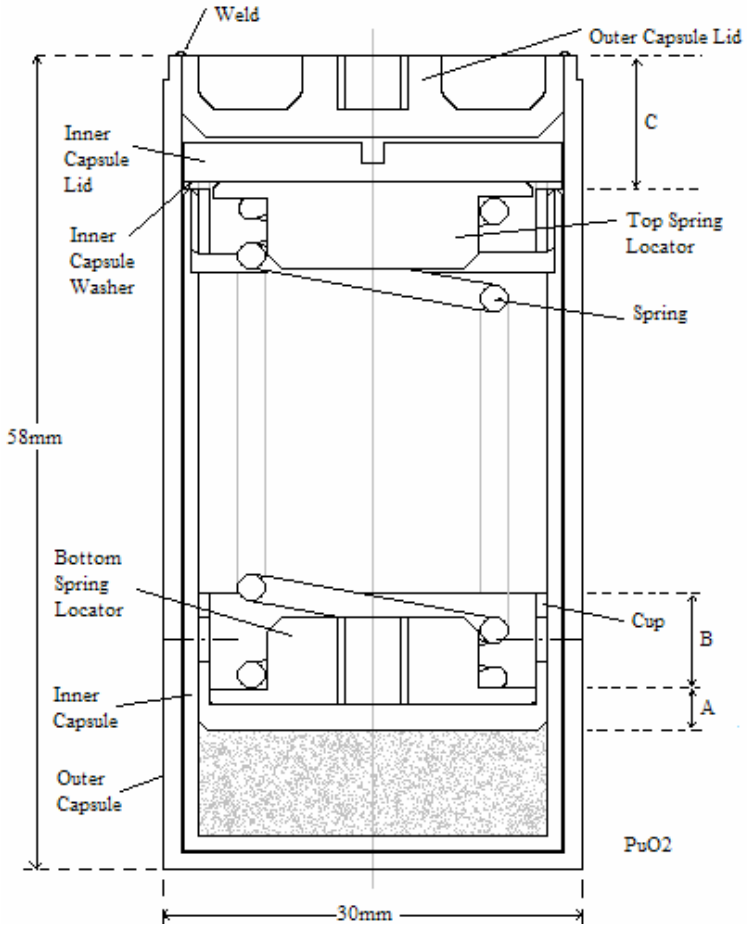

Figure 10: The AE4043/nn source internal capsule components and basic dimensions, re-sketched from Crossley et al, 1991 [45].

Table 3: AE4043/nn source Pu and PuO_2 content and calculated fill heights assuming a density of 1.856 g.cm^{-3}.

Source ID	PuO_2 mass (g)	Pu mass (g)	Fill height (mm)
AE4043/1	0.113	0.099	0.12
AE4043/2	0.565	0.494	0.62
AE4043/3	1.128	0.986	1.24
AE4043/4	2.261	1.977	2.48
AE4043/5	5.650	4.941	6.20
AE4043/6	8.479	7.414	9.31
AE4043/7	11.298	9.879	12.40
AE4043/8	22.597	19.758	24.80
AE4043/9	28.246	24.697	31.00
AE4043/10	28.252	24.702	31.01

The source sizes used in this work range from 0.099 g to 24.70 g of Pu (0.11 g to 28.25 g of PuO_2) as shown in Table 3. This table also contains an estimate of the PuO_2 fill height within the inner capsule based upon a density of 1.856 $g.cm^{-3}$; however the true density of the powder is not specified. From the original sketch and micrometer measurements (Figure 10) the internal diameter of the inner capsule is accurately 25 mm, the inner capsule is 1.11 mm thick, the outer capsule is 1.14 mm thick and the gap between the two capsules is 0.25 mm.

3.3.1 AE4043/nn Preliminary Source Measurements

Two identical sets of measurements have been performed using a single 70 mm diameter by 20 mm thick BEGe3820 detector, to observe the behaviour of the SAC algorithm for the AE4043/nn sources whilst not within drums or waste matrices. The apparatus was constructed on a horizontal bench, as shown in Figure 11, so that the active source material was approximately level with the centre of the detector, with the relevant edge of the source casing at 40cm and 43cm from the detector. The AE4043/nn sources were measured in two different orientations: upright (as shown with the active material at the base) and horizontally (on their side with the active material nearest to the detector). The sources were separated from the detector with a 1.5 mm thick Cd attenuator sheet to reduce the high count rate from the lower energy gamma rays especially the intense 60 keV radiation from ^{241}Am which grows in from the decay of ^{241}Pu.

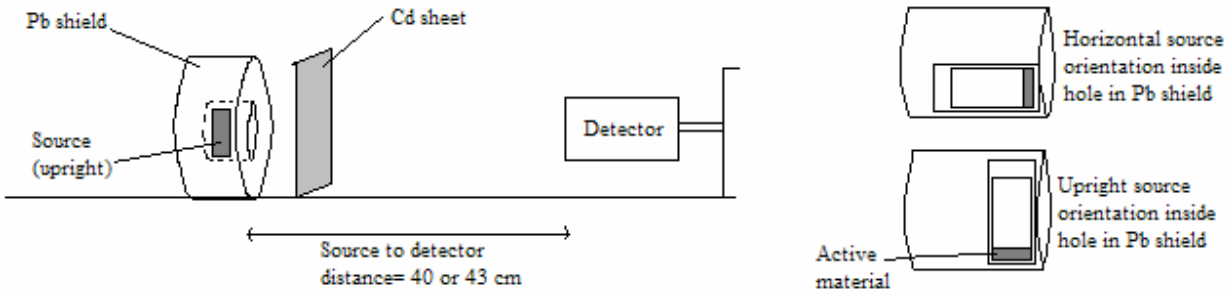

Figure 11: AE4043/nn sources preliminary test measurements with source in the upright position.

Energy and efficiency calibrations were performed with a multi-line (^{241}Am, ^{133}Ba, ^{137}Cs, ^{152}Eu) source and a reference pulser was used to perform the deadtime correction. The 129 keV and 414 keV apparent mass results are plotted in Figure 12 and Figure 13 respectively for both measurement sets and source orientations, including measurement errors.

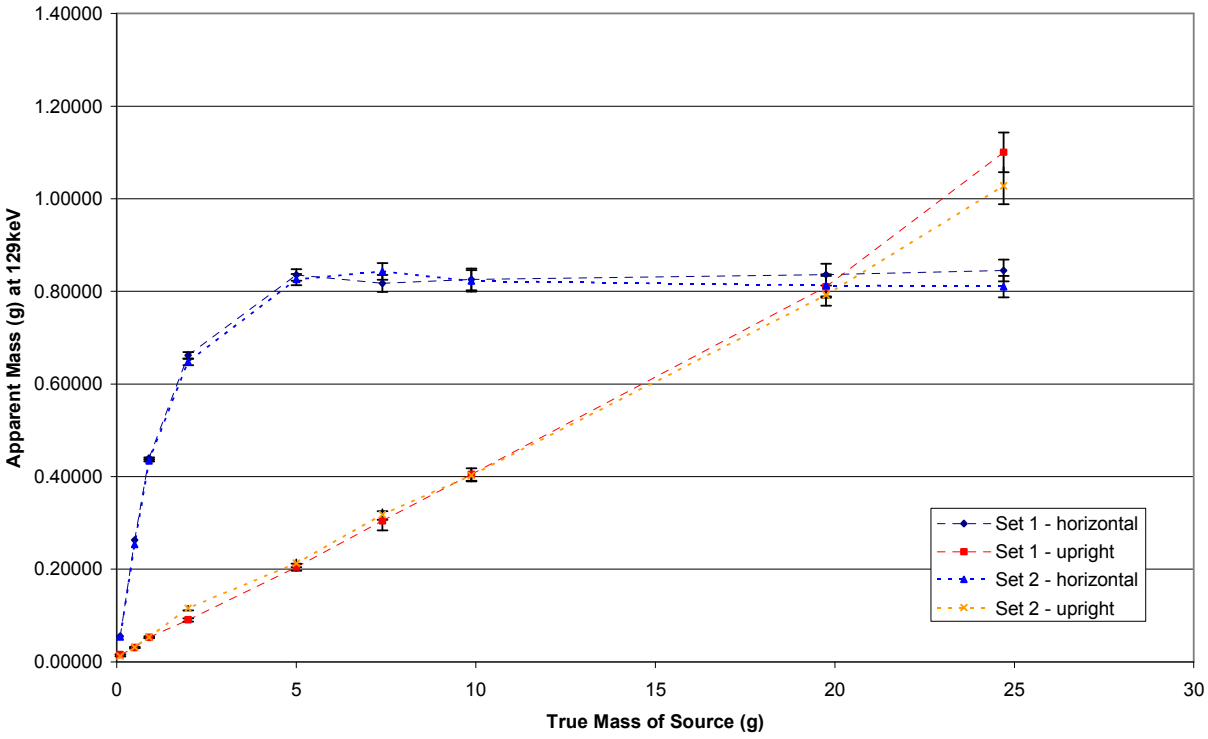

Figure 12: Graph showing the measured apparent masses for two sets of measurements at 129keV for the AE4043/nn sources for both horizontal and upright source orientations.

For the sources orientated in the upright position, with the axis of the source material normal to the detector axis, the thickness of PuO_2 seen by the detector remains constant as the mass (and fill height) increases. Consequently the apparent masses of the 129 keV and 414 keV lines increase linearly (allowing for statistical fluctuations) in direct proportion to the fill height assuming that the bulk density is constant for all sources (see section 3.3.2). For the sources lying horizontally with the circular base at right angles to the detector axis, the apparent mass of PuO_2 increases with source mass until the gamma-rays can no longer penetrate the PuO_2 on route to the detector. For

the 129 keV lines this occurs at a source mass of approximately 5g (apparent mass 0.83 ±0.16 g). Figure 13 demonstrates that the 414 keV gamma rays do also suffer from the effect but much less strongly.

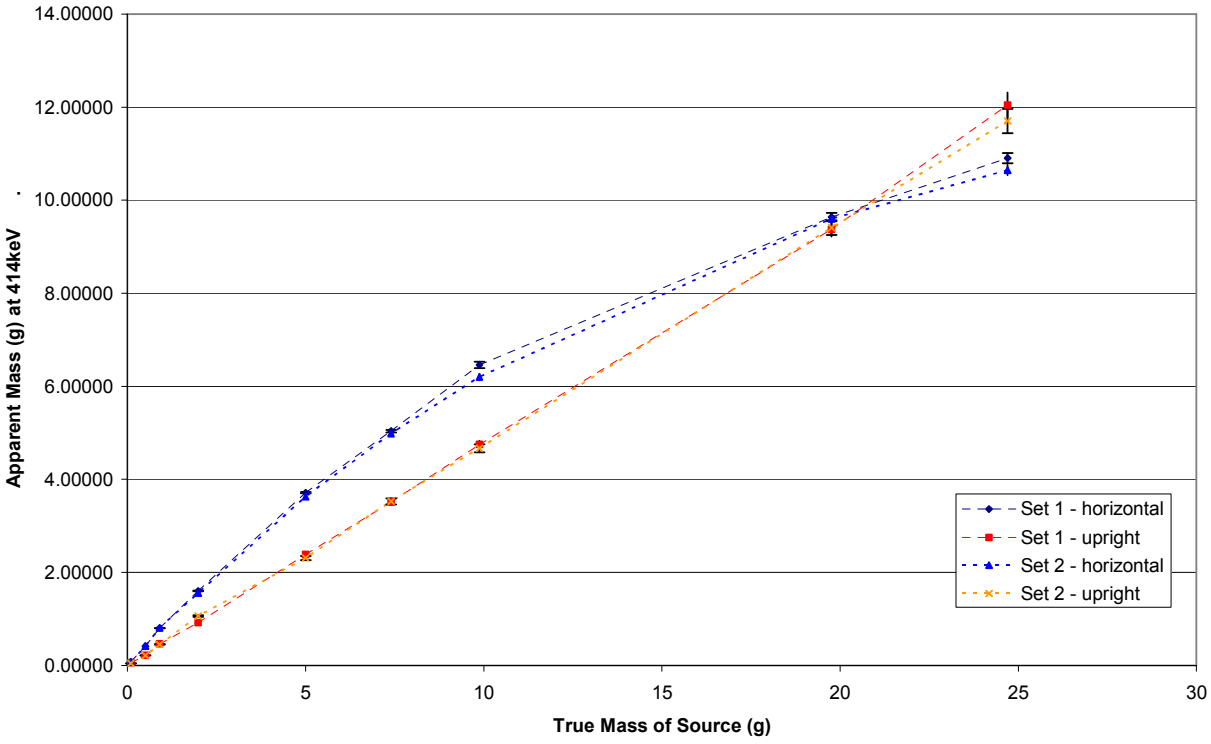

Figure 13: Graph showing the measured apparent masses for two sets of measurements at 414keV for the AE4043/nn sources for both horizontal and upright source orientations.

3.3.2 AE4043/nn PuO_2 Density Determination

In order to be able to model the sources correctly, the density of the PuO_2 inside the inner capsule of the AE4043/nn sources must be known. Despite the detailed mechanical descriptions of the sources, the fill heights and densities of the source PuO_2 powder have not been stated.

Previous studies at Canberra by Croft et al [46] have assumed a density of 1.51 g/cm^3 for all sources, estimated assuming that the PuO_2 powder in AE4043/9 and /10 fills the inner capsules since their springs are not present. These studies were later revisited [47] and densities between

1.72 g/cm^3 and 2.03 g/cm^3 were adopted for the sources based upon assumptions about the length of the spring which holds the cap in place.

In order to better estimate and independently confirm the density of the AE4043/nn sources the fill-height of a selection of sources must be determined from experimental data [48]. An experiment has been set up for this purpose, as shown in Figure 14.

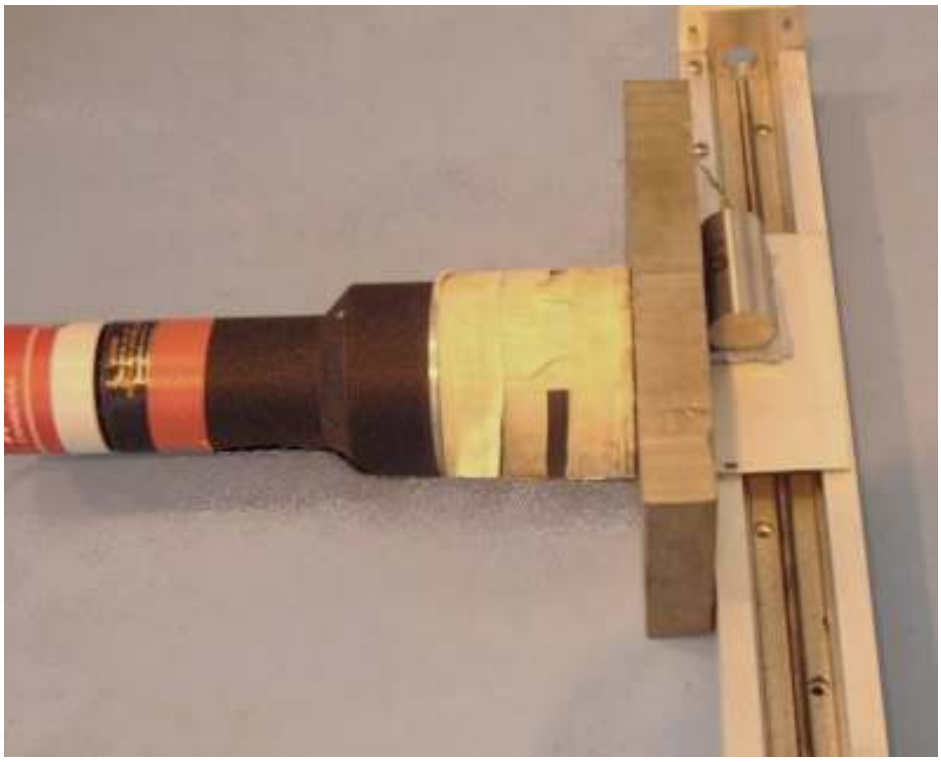

Figure 14: Photograph of the machine slide experiment used for powder distribution and fill-height measurements of the AE4043/nn sources.

The equipment consists of a 7cm diameter NaI detector connected to a Canberra UniSpec MCA, set perpendicular to a machine slide, and separated from the source by a 30 mm deep tungsten collimator with a 1 mm hole. The instruments are secured to the table so that the source detector and machine slide cannot move independently (not shown in the figure). The initial source position is beyond the view of the detector through the collimator and is moved in 0.25-0.5 mm

intervals using the manually-operated machine slide so that the side of the source passes along the sight of the collimator, until the measured countrate returns to its original value and remains at this level for several measurements.

The deadtime-corrected counts in the 60 keV peak region of interest (ROI) (from ^{241}Am) are recorded for regular periods (the duration depends on source strength) using Genie^{TM} 2000 Gamma Acquisition and Analysis [49]. The 60 keV peak has been chosen since it has a high intensity and is at a relatively low energy and so will not be affected by the collimator as much as any higher-energy peaks.

For the purpose of this experiment it is assumed that at the very edge of the active material the collimated detector will observe half of what it would observe for an infinite material because the edge of the source is exactly half way across the collimator gap. Consequently the FWHM of the spatial count rate profile should give an estimate of the thickness (height) of active material in the source. In order for this assumption to apply the spatial profile must also reach a definite peak region so the FWHM may be correctly calculated. Therefore the source must be of sufficient height so that a flat region is observed where the countrate is unaffected by the edges of the active material. Calculations show that the field of view of the source from the detector is approximately 1.4mm and so the measured source must have a fill height greater than this value. Consequently, this process has been performed for 6 sources: AE4043/5, 6, 7, 8, 9 and 10 (approximately 5g, 7.5g, 10g , 20g, 25g and 25g respectively) (see Table 5). An example of the spatial profile for AE4043/6 is shown in Figure 15.

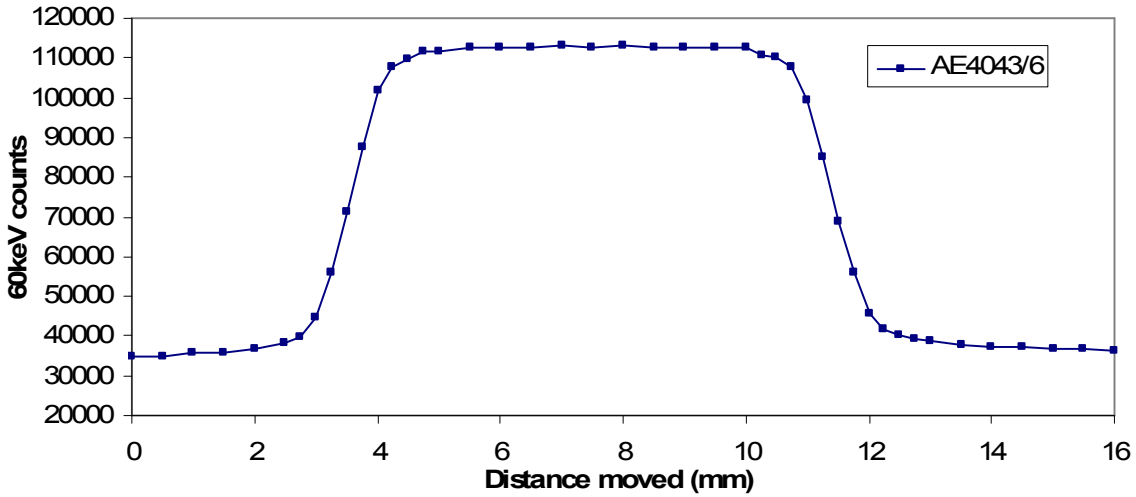

Figure 15: Spatial profile for 60 keV activity distribution in the 7.5 g AE4043/6 source.

To calculate the density of the PuO_2 in the source the FWHM of the distribution must first be found. For this example (Figure 15) the background countrate is averaged at 35500 counts, and the peak counts are averaged at 112800 counts. Therefore the Half Maximum value is 74150 counts (after accounting for the background) and it can then be determined between which two pairs of source locations the FWHM should be calculated. It is assumed that the graph is linear between the pair of the points and so by plotting the straight line and using the Half Maximum value as the co-ordinate the FWHM may be determined. Table 4 and Figure 16 show the results for four of the six sources. The remaining two sources have been omitted as explained below.

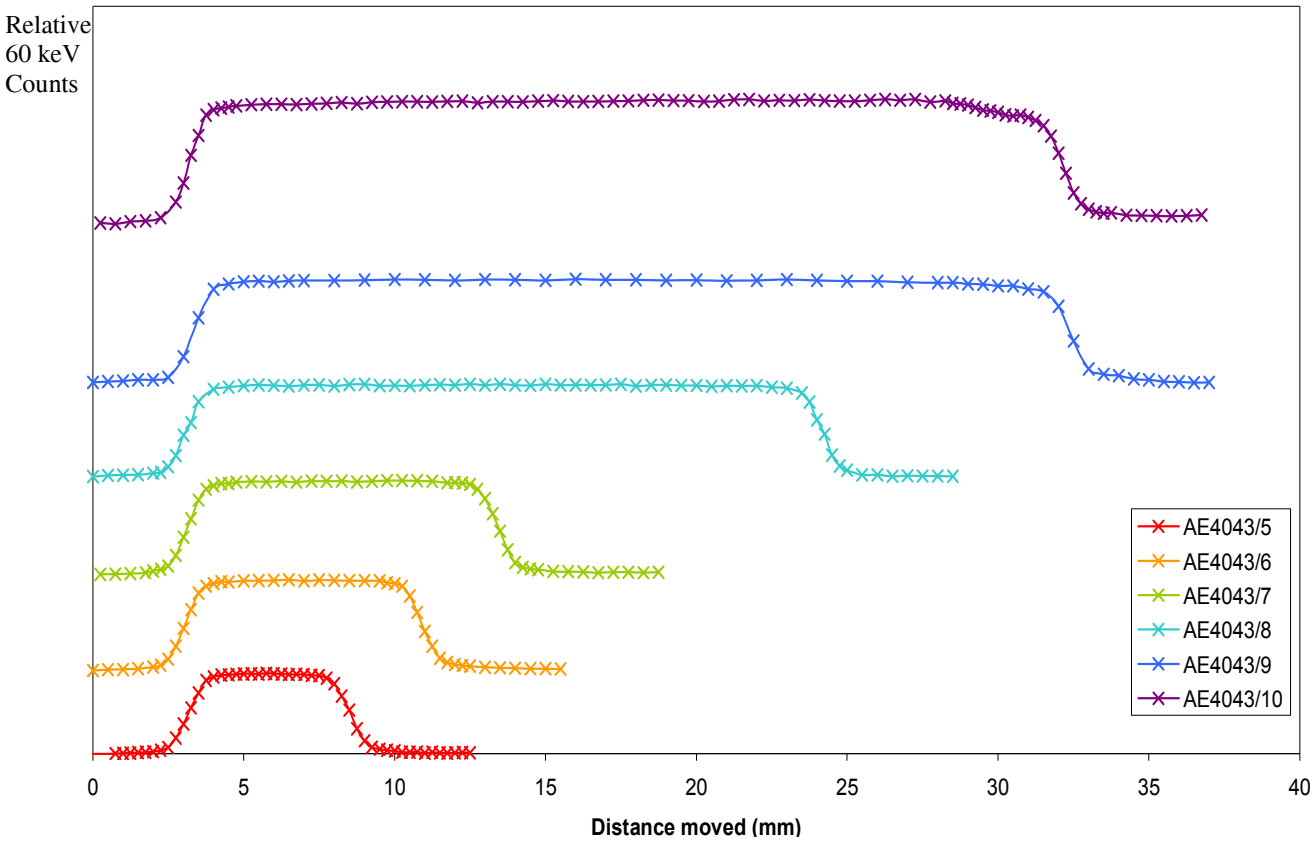

Figure 16: Graph showing the relative 60 keV counts versus the distance moved for sources AE4043/5-10.

Table 4: AE 4043/5, 6, 7 & 8 measured FWHM and calculated densities using a NaI detector and Canberra Unispec.

Source	FWHM = fill height (mm)	Mass of PuO_2 (g)	Calculated Density ($g.cm^{-3}$)	Uncertainty ($g.cm^{-3}$)
AE4043/5	5.390 ± 0.14	5.56	2.14	0.11
AE4043/6	7.876 ± 0.14	8.48	2.20	0.05
AE4043/7	10.310 ± 0.14	11.30	2.23	0.03
AE4043/8	21.092 ± 0.14	22.60	2.18	0.01

The heights of the maximum and minimum flat regions have been calculated using an average of all data points at this level and so their error is treated as negligible. Similarly, since the gradient is determined from the nearest two points then the gradient uncertainty is neglected. The FWHM uncertainty is calculated as the quadrature summing of the statistical measurement uncertainty ($\sqrt{N}$ where N is the number of counts) and the uncertainty in the location of the machine slide

(approximately 0.1 mm). The uncertainty in the density is then calculated by propagating through the uncertainty in the FWHM.

In some of the sources measured there is a small difference in start and end values, which may be due to the cap having a small groove along its outer edge, designed to allow air to flow out whilst it is being put in place, or may be due to loose powder residing above the cap if the inner capsule was contaminated during assembly. It should also be noted that these measurements were not background subtracted since an ROI was used to determine the 60keV counts rather than using the net peak area. Consequently the background may increase as the source is moved to a position where coherent scattering could affect the number of counts reaching the detector. Similarly if the side of the source was not completely parallel to the detector face then the flat top of the profile may appear to rise or fall as the source is scanned. Where a difference in start and end values is observed an average of the start and end value (the background level with the collimator not viewing the source) has been used as the background signal in the density calculations.

The results indicate that the PuO_2 powder inside the capsules have an average density of ~(2.19±0.04) $g.cm^{-3}$. However, it appears from the lower three results that the density is increasing with mass. This may be since the cap which holds the powder in place is held down by a cut spring. The uncompressed length of the cut springs is not documented. As the fill height increases there may more pressure from the spring and so the powder may be more compressed. However, observations of data from Figure 13 indicate that the 414 keV apparent mass behaves linearly with mass and so it is assumed that the density is approximately constant through the set of sources.

Observations of the spatial profile of the AE4043/10 (approximately 25g Pu) source (and AE4043/9 to a lesser extent) indicate that the internal geometry of the source is different to the others and so this result is not valid for the purpose of an average density estimation.

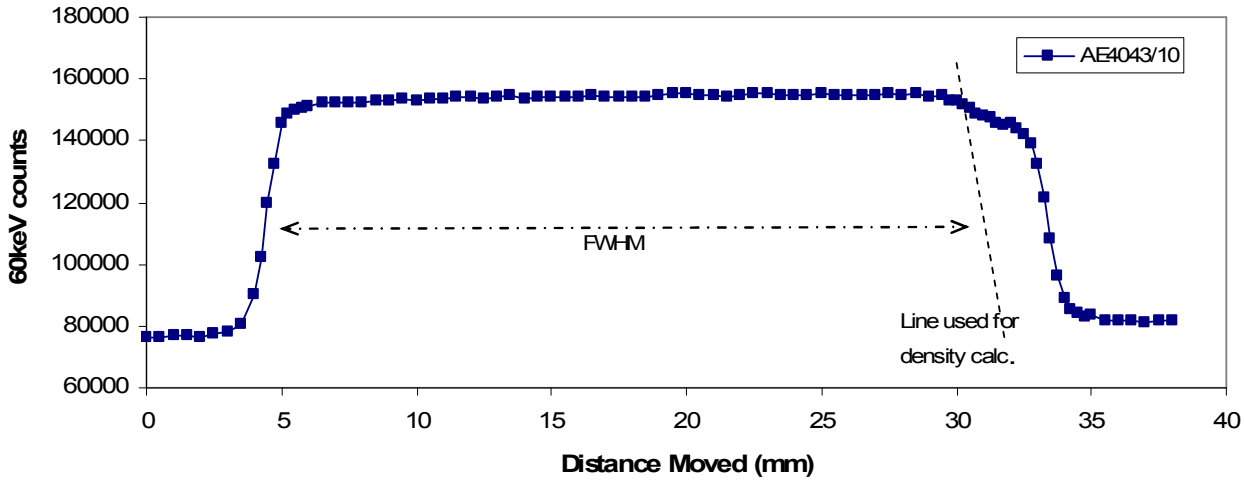

Figure 17: Spatial profile for 60 keV activity distribution in the 25 g AE4043/10 source.

The number of 60 keV counts versus distance moved graph for AE4043/10 is shown in Figure 17. The number of 60 keV counts rises similarly to the other sources, however the descending curve behaves somewhat differently; there is an initial slower decrease in the number of counts from 30 mm to 33 mm and then the number of counts decreases to a value slightly higher than the initial background level. This initial decrease may be due to the fact that this higher mass source does not contain a spring to hold the cap in place and so it is possible that the cap may have moved, allowing the PuO_2 powder to move more freely at the top of the capsule, and hence be less dense than the main body of powder.

To calculate the density of the main body of PuO_2 powder of the AE4043/10 source it has been assumed that the FWHM can be taken from the half maximum on the ascending line and the half maximum at an imaginary line drawn from where the countrate initially starts to descend. This assumption will give an approximate density of 2.17 $g.cm^{-3}$, whereas using the plotted descending line gives an average density of 1.99 $g.cm^{-3}$. A similar analysis of the AE4043/9 source gives 2.08 $g.cm^{-3}$ and 1.98 $g.cm^{-3}$ respectively.

3.3.3 AE4043/nn Powder Distribution Measurements

Previous testing of the AE4043/nn sources has shown the AE4043/1 source to have a consistently low mass of approximately 55 mg by gamma assay [50]. The cause of the low measured Pu mass

for the AE4043/1 sample may be a result of an asymmetrical Pu powder distribution, or the powder may reside within a ring on the outer diameter of the inner capsule due to the small fill-height, held in place by the raised edge on the base of the cup (see Figure 10). An experiment was set up to test this hypothesis.

The experimental set-up is similar to that shown in Figure 14 except that the source is rotated horizontally by 90^{o} so that the base of the source container is parallel to the flat surface of the detector. The 60 keV count rate is observed across the base of the AE4043/1 in two dimensions (i.e. by rotating the source about its axis 90^{o} and re-measuring) and the AE4043/5 serves as a control case to observe the expected behaviour for a source with uniformly-distributed activity. The resulting profile for the 5g source is shown in Figure 18 and demonstrates a symmetrical powder distribution. The profile is a dome shape since as the collimator is moved across the base of the capsule the visible chord length (y) increases as a function of the apothem (x) (or distance moved across the source) until the diameter length (R/2) is reached at the central position, and then decreases symmetrically using the equation below:

$$y = 2\sqrt{R^2 - x^2} \qquad \textbf{Eqn. 11}$$

This equation has been normalised to the measured curve and plotted in Figure 18 to demonstrate the expected behaviour or the spatial profile. The two curves are equal when allowing for statistical fluctuations and so the AE4043/5 source may be assumed to be symmetrical with uniform PuO_2 powder distribution across the base of the capsule.

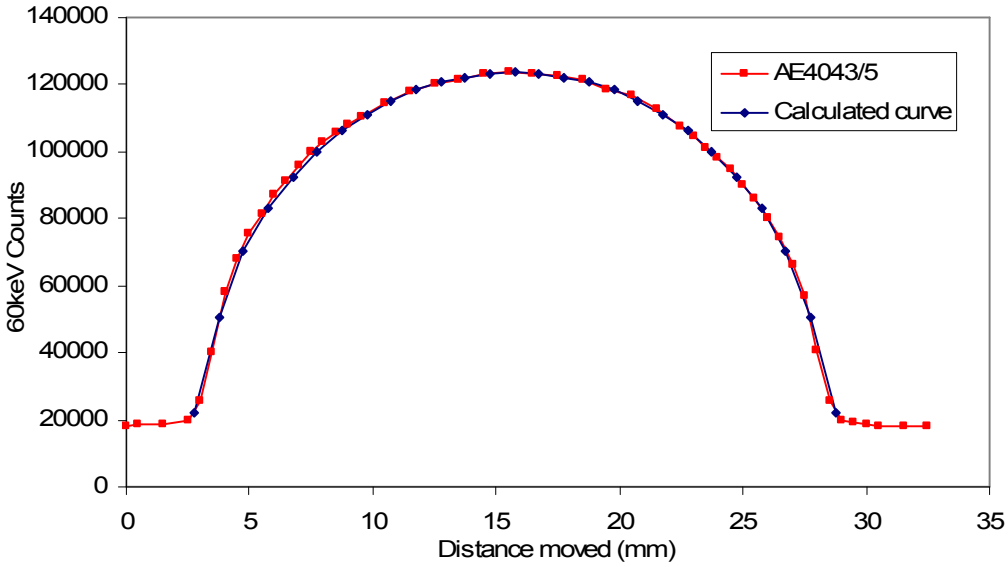

Figure 18: The 60keV profile of AE4043/5 across the base demonstrating uniform PuO_2 powder distribution.

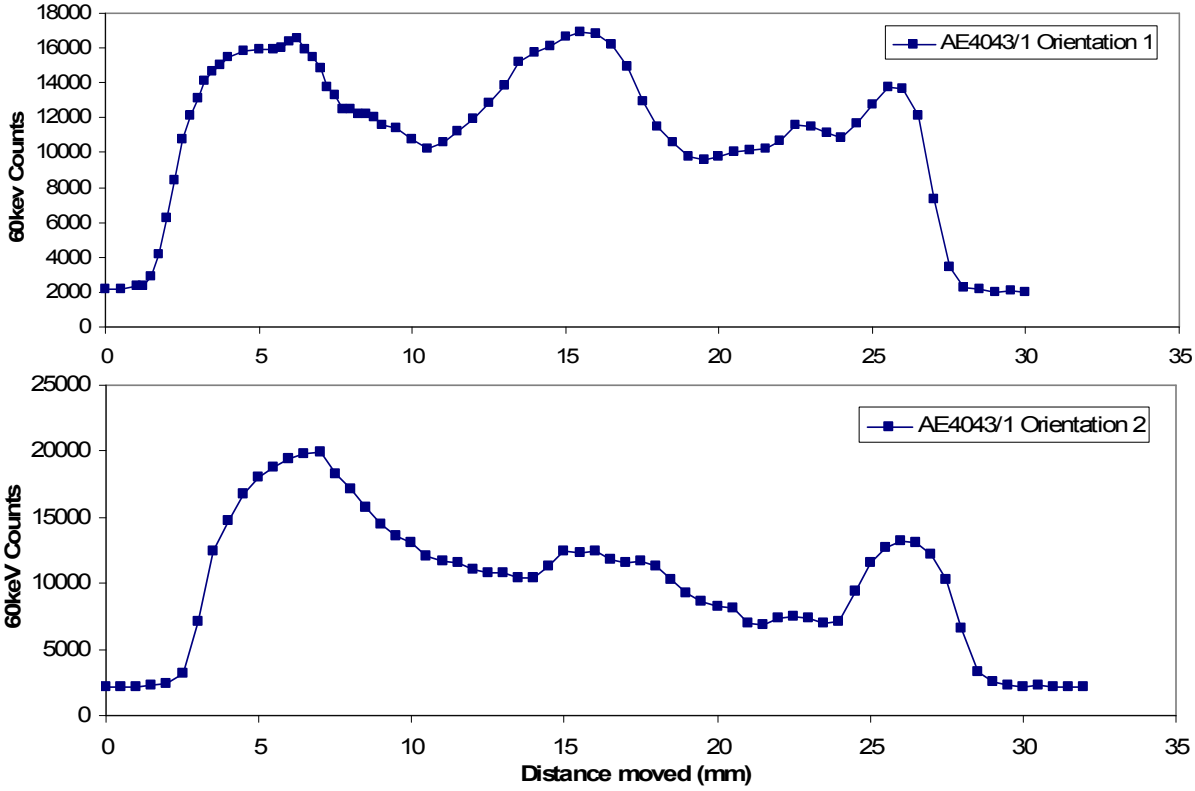

Figure 19: The AE4043/1 source 60 keV profile across the base of the source in 2 different orientations.

The profile for the AE4043/1 source is shown in Figure 19 for two different orientations with the source rotated about its axis by 90°. The number of counts for the two orientations is different in the centre since the source was not at a consistent distance from the detector and collimator; however the base of the source was set parallel to the collimator and detector face in each situation. The spatial profiles show that the activity is neither symmetrical nor uniform across the base of the capsule. The active material appears to reside mostly in the rim area around the outer edge of the inner capsule, with a possibly a small amount of active material remaining in the inner section.

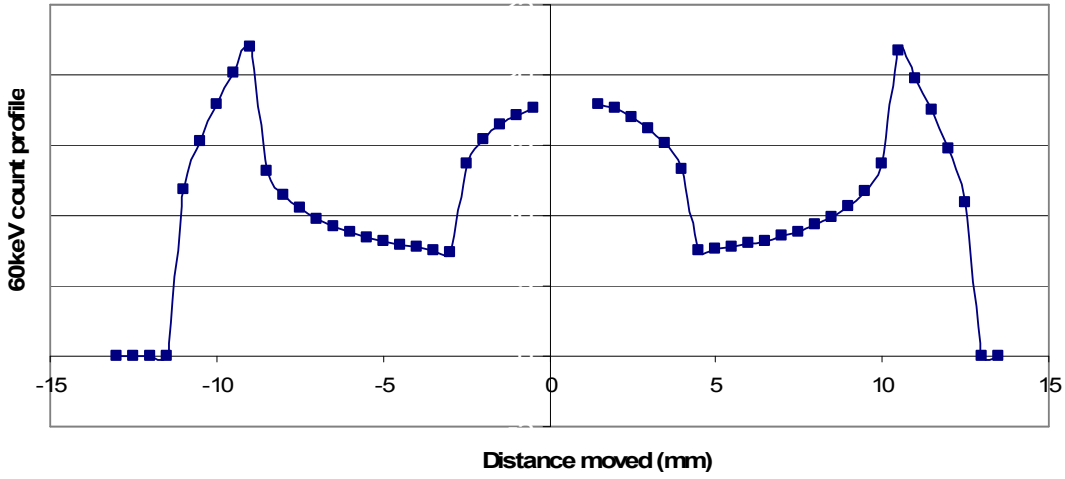

Figure 20: Expected 60keV spatial profile for a uniformly thick source consisting of active powder in a 2.5mm thick ring around the outside plus a 4mm radius circle in the centre.

Figure 20 demonstrates an example of the calculated spatial profile for a source consisting of a 2.5mm thick ring of active powder around the outside of the cap plus a 4mm radius circle of powder in the centre (where all powder has an equal fill height). The measured profiles are far less symmetric and the powder appears to be more randomly distributed across the central section, indicating that the PuO_2 powder may be mobile below the cap within the capsule. To test this, the AE4043/1 source has been measured in the same orientation a further two times after the source has been tapped gently on the left (Figure 21: Measurement 1) and the right (Figure 21: Measurement 2) i.e. at 90° either side of the measured orientation.

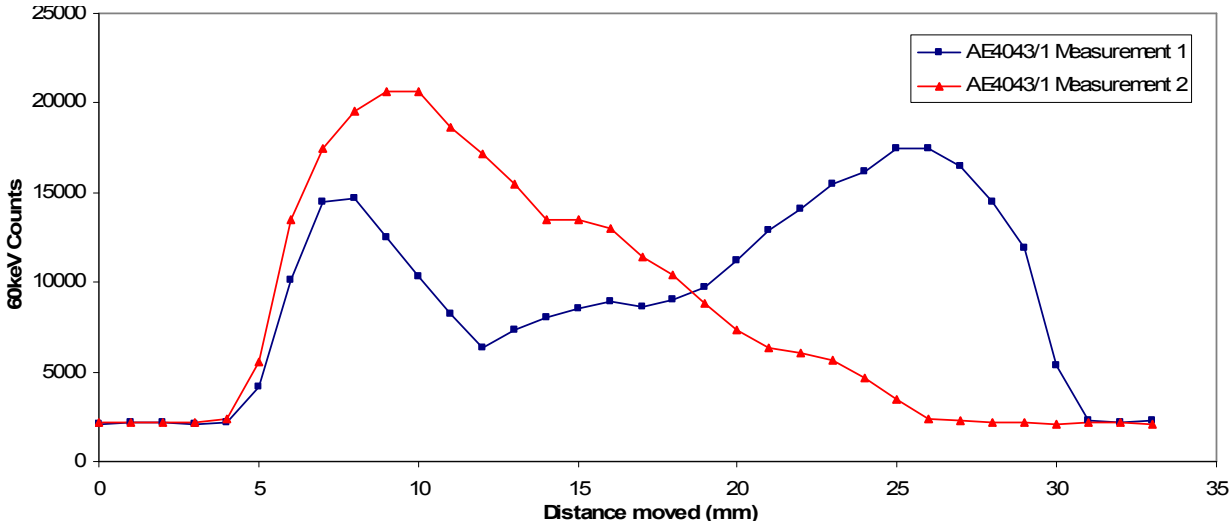

Figure 21: AE4043/1 counts across the base of the source after gently tapping the capsule on either side.

Figure 21 shows a clear difference between the two measurements. In each case the powder appears to have moved towards the lower side whilst tapped. The second "tapping" has caused the powder that once resided around the outer ring to slip to the opposite side. Consequently, due the unpredictability of this source it shall be omitted from future modelling and measurements.

3.3.4 AE4043 Modelling

Selected AE4043/nn sources (omitting sources AE4043/1, 9 and 10) have been modelled using the point source model to support the density and fill height measurement results in the previous section, and to assist in validating the point source model.

Table 5: AE source Pu and PuO_2 content and calculated fill heights assuming a density of 2.19 g.cm^{-3}.

Source ID	PuO_2 mass (g)	Pu mass (g)	Fill height (mm)
AE4043/2	0.565	0.494	0.53
AE4043/3	1.128	0.986	1.05
AE4043/4	2.261	1.977	2.10
AE4043/5	5.650	4.941	5.26
AE4043/6	8.479	7.414	7.89
AE4043/7	11.298	9.879	10.51
AE4043/8	22.597	19.758	21.02

The PuO_2 density is assumed to be 2.19 g/cm^3 (as determined in section 3.3.2), and the material is uniformly distributed (excepting sources AE4043/1, 9 and 10 - see section 3.3.3). From these assumptions the thickness of the PuO_2 powder may be calculated as being in the range 0.1 mm to 26.3 mm (see Table 5).

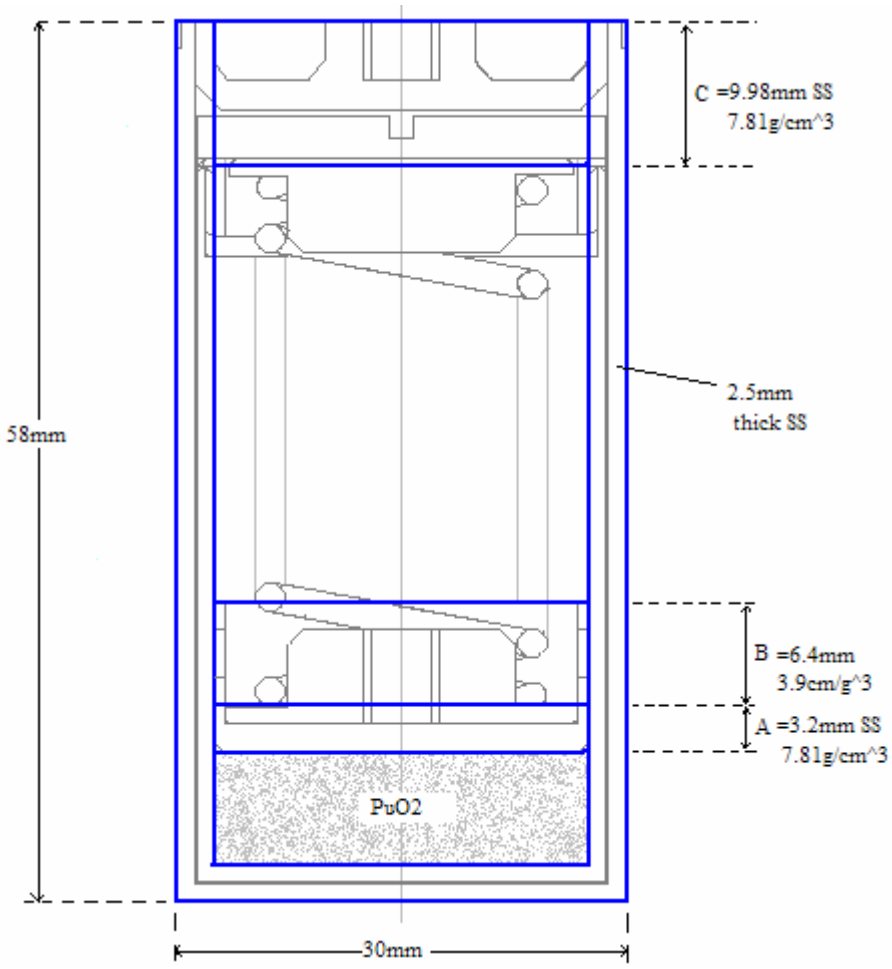

Figure 22: AE4043/nn source showing blue lines for the modelled set-up.

The stainless steel (SS) is modelled using the Genie 2000 ISOCS MuEditor program as:

- C: 0.08%
- Cr: 19.0%
- Fe: 71.92%
- Ni: 9.0%

with a density of 7.81 g.cm^{-3}. The AE4043/nn source is modelled as shown by the blue lines in Figure 22. Areas A and C and the outer encapsulation are modelled as solid SS. Area B has been modelled as SS with half the normal density, 3.905 g.cm^{-3}. Due to the manufacture process of the sources all Pu powder should reside within the area below the cap in the inner capsule, and the powder should be distributed symmetrically within this area. The sources have been modelled with this distribution, with the fill heights stated in Table 5.

The detector has been modelled as a 7 cm diameter, 2.1 cm thick uncollimated detector at 40cm from the source, to mirror the experimental set-up. The ratio of attenuated to unattenuated counts have been recorded for the 129 keV and 414 keV lines for the 7 selected sources.

Preliminary results show that for both lines the modelled results are larger than the measured results taken from the AE4043/nn Preliminary Source Measurements (section 3.3.1). However, there are a number of factors which could bias the measured and modelled results. For example the measured results depend on the accuracy of techniques such as the efficiency and deadtime corrections, and nuclide library parameters such as the branching ratio of the lines. If these are not accurate then the modelled and measured results will differ. The modelled results also may be affected by encapsulation assumptions, the estimated average density or the value of the attenuation coefficient (μ) used. These preliminary results use a value of μ as set by Genie ISOCS (see section 2.2) which neglects coherent scattering. The modelling has been repeated with μs from the XCOM database [15] both with and without coherent scattering (see Figure 23).

For all sets of results the plots “dip” for the 5 g source. This may be due to an anomaly in the measured dataset. Also the smaller sources appear to have a lower measured to modelled ratio; this may be a consequence of a non-uniform density across the set of sources.

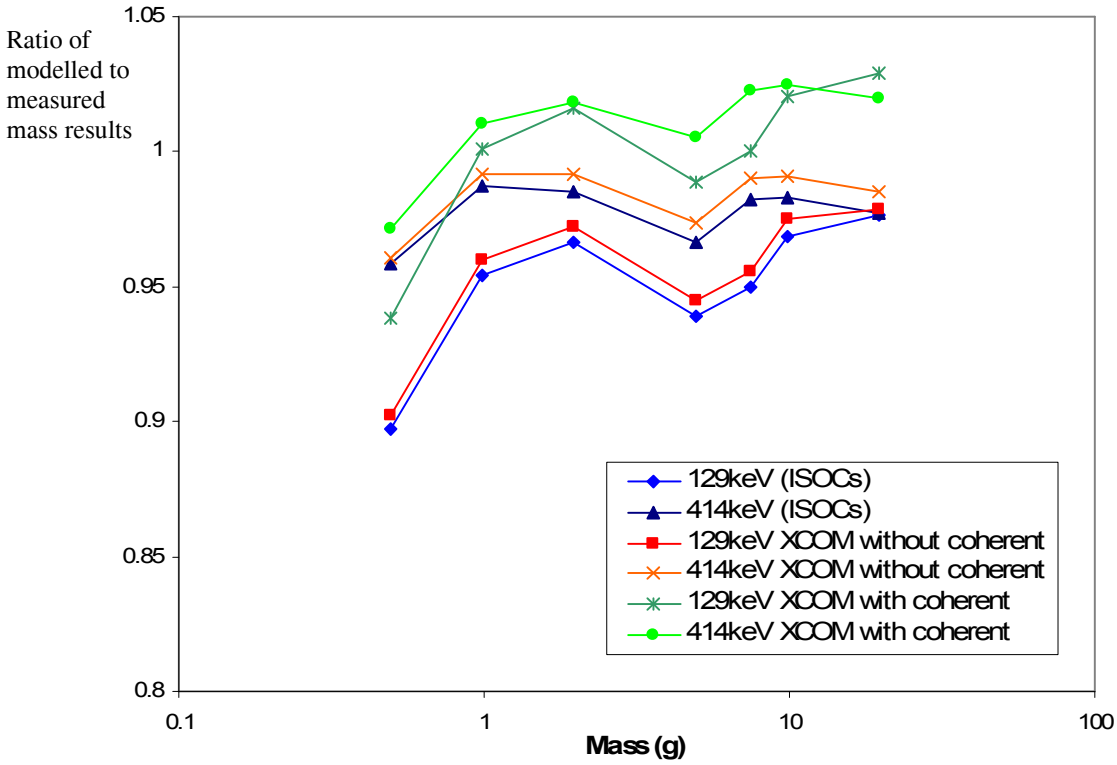

Figure 23: Graph showing the measured (from Preliminary Source Measurement data, see section 3.3.1) to modelled mass ratio for selected AE4043/nn sources for the 129 keV and 414 keV lines for different μs.

The results show that the XCOM μ without coherent scattering, although improving the measured to modelled ratio compared to that for the original Genie ISOCs μ, still produces modelled results which are too large, whereas, on average the XCOM μ with coherent scattering produces modelled results that are slightly too small. This is since if the μ includes coherent scattering the attenuation coefficient (and collision cross-section) is larger and so the apparent mass calculated by the model will be smaller. Physically the apparent μ (the μ that should be used in the model to produce the result that you would obtain with all the scattering in the real sample) may lie somewhere between the two values since the attenuation coefficients do not take account for situations where the gamma ray is initially not directed towards the detector but is coherently scattered towards it. It would be possible to determine the true μ by modelling the geometrical set-up of the experiment, including surrounding objects and equipment, using complex models such as MCNP, however this has not been performed since the benefit of the results would not be significant for the purposes of this thesis.

The XCOM μ with coherent scattering will be used since the individual 129 keV and 414 keV apparent mass results are nearest to the measured results out of the studied μ types.

3.4 Fleissner Method Analysis

3.4.1 The Two-Line Method

The behaviour of bare Pu cylinders (i.e. not encapsulated within stainless steel) of diameter equal to height have been calculated with the point source model using the basic two-line (129 keV and 414 keV) Fleissner method for three different densities: pure Pu at ρ = 19.8 g.cm^{-3}, PuO_2 at ρ = 1.856 g.cm^{-3} and PuF_3 at ρ = 7.1 g.cm^{-3}, over the mass range 0.1 mg to 200 g. In the model it is assumed that the cylinder is viewed in the far field by a detector located along a mid-plane diameter.

The parameters for the bare Pu cylinders are inputted and the total (uniform source) counts rates are determined. The calculation is then repeated with the density in the attenuation function set to zero. The ratio of these two results gives the self-attenuation factor (SAF_i of the i'th energy). The apparent mass (M_i of the i'th energy) is then calculated as:

$$M_i = SAF_i M_{TIn} \qquad \textbf{Eqn. 12}$$

where M_{TIn} is the inputted true mass of the cylinder. The simplified Fleissner equation:

$$M_i = M^o e^{-\beta/E_i} \qquad \textbf{Eqn. 13}$$

may be rearranged using the 129 keV and 414 keV lines to show that the model parameter, β, may be given by:

$$\beta = \frac{\ln\left(\frac{M_{129}}{M_{414}}\right)}{\left(\frac{1}{414} - \frac{1}{129}\right)} \qquad \textbf{Eqn. 14}$$

and hence:

$$M^o = M_{129}.e^{\frac{\beta}{129}} = M_{414}.e^{\frac{\beta}{414}} \qquad \textbf{Eqn. 15}$$

where M^o is the Fleissner method corrected mass. The over-correction (the ratio of the corrected mass to the true mass for the basic Fleissner method) is displayed on Figure 24.

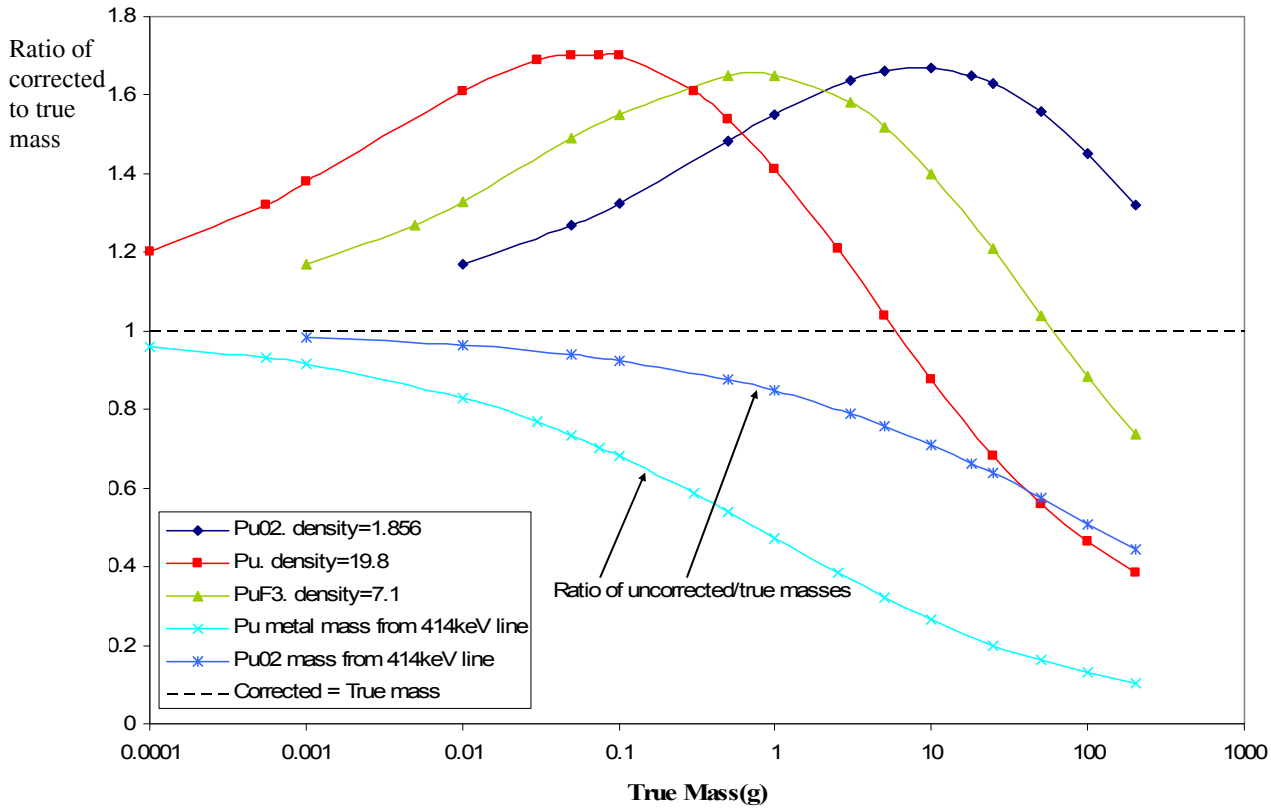

Figure 24: The basic Fleissner SAC mass versus True mass for Pu Metal, PuO_2 and PuF_3 cylinders.

The graph shows that the default Fleissner method not only over-corrects by a factor of 1.5 at intermediate masses, but also severely under-corrects at higher masses for Pu metal lumps. For example, a 100 g Pu metal lump would appear as only 50 g, a 50% under-determination. In many routine waste assay situations this is not a serious concern because the maximum single lump size is expected to be far smaller than this. For example, in fabrication facilities the waste is restricted to items such as fine oxide powder, grindings and pellet chips. Similarly in a glove box clean-out exercise visual inspection, screening and packing records are often available to confirm maximum lump size. However, historical waste from weapons production facilities may pose particular concern since records may be incomplete.

The graph also shows curves that would be obtained from the 414 keV line with no SAC correction. These curves indicate that for a range of masses (particularly below 100 mg for Pu

known to be in the form of oxide) it might be better to offer no correction at all rather than to use the Fleissner 2-line approach.

3.4.2 The Three-Line Method

The three-line Fleissner method has been calculated for bare Pu cylinders of diameter equal to height inside a stainless steel (1.6 mm thick) drum using the 129 keV, 375 keV and 414 keV lines of ^{239}Pu. The point source model has been used in the same manner as for the two-line Fleissner method to determine the apparent mass of the three lines (129 keV, 375 keV and 414 keV). The full Fleissner equation has been rearranged as:

$$f(M_0, \alpha, \beta) = M^0 - M_i\left(1 + \alpha\left(e^{-\beta/E_i} - 1\right)\right)^{-1} = 0 \qquad \textbf{Eqn. 16}$$

to determine values for α (constrained to be ≤1), β and hence M_0 using a numerical technique. If it is assumed that the data is well behaved and a solution exists we may suppose that:

$$f(M^0 + \delta M^0, \alpha + \delta\alpha, \beta + \delta\beta) = \varepsilon_i \qquad \textbf{Eqn. 17}$$

then a solution must be found where:

$$\delta\left(\sum_i \varepsilon_i^2\right) = 0 \qquad \textbf{Eqn. 18}$$

This has been performed by incrementing each parameter M^0, α and β in turn and finding the minimum value of $\sum_i \varepsilon_i^2$. The corresponding M^0, α or β is then set as an input parameter and the process iterated until $\sqrt{\sum_i \varepsilon_i^2}$ reaches a value less than 5% of the value of M^0.

During this process it was found that the determined parameters would not settle where α was less than 1 since the absorption in the modelled lump is entirely due to the self absorption within the sample and thus the method reduces to the 2-line Fleissner method, as studied in the previous section.

A graph showing $\alpha e^{-\frac{\beta}{E_i}} + (1-\alpha)$ and $e^{-\mu\rho x}$ for an arbitrary thickness, x, has been plotted as a function of energy in Figure 25. The plotted α-constrained $\alpha e^{-\frac{\beta}{E_i}} + (1-\alpha)$ has used an α of 0.9 and β of 200. Although it may fit the $e^{-\mu\rho x}$ curve at 414 and 375 keV it can not fit the curve at 129 keV. If the value of α is unconstrained it offers the best fit to the $e^{-\mu\rho x}$ curve at the three energies with α ~ 1.013 and β ~ 120.

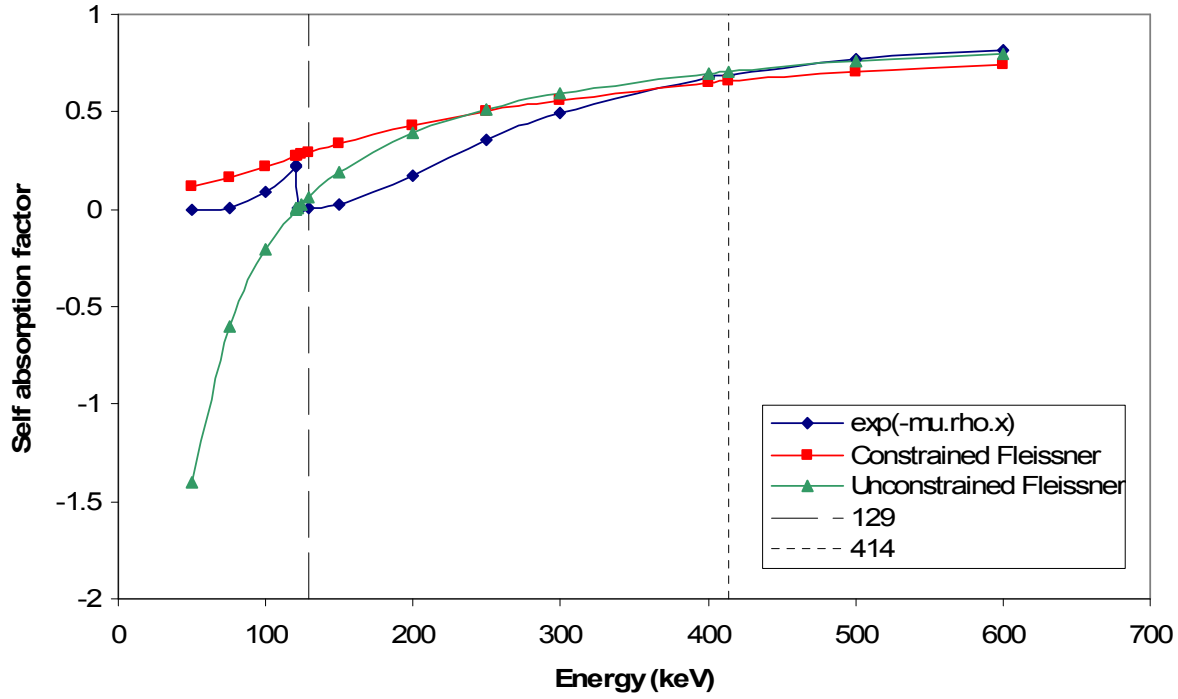

Figure 25: A graph comparing $\alpha e^{-\frac{\beta}{E_i}} + (1-\alpha)$ with constrained and unconstrained α as a function of energy compared to $e^{-\mu\rho x}$.

Since it has been found that the attenuation curve (at 129 keV and 414 keV) may best be fitted with an unconstrained value of α, the corrected mass has been determined using the 3-line Fleissner equation with this method. Using the unconstrained parameters the value of β was found to remain close to 1.01, whereas α increases steeply until approximately 5 g and then converges to 121.3 (for Pu lumps) and 120.1 (for PuO_2 and PuF_3 lumps), as shown in Figure 26. This value of α

is far from unity and indicates that the assumption that made by the 2-line method is a poor approximation. However, in physical reality α =1 should be correct since all the Pu is subject to self-absorption.

The ratio of the corrected mass to the true mass for the modelled data is illustrated in Figure 27. The 3-line method is shown to perform much better than the 2-line approximation for smaller masses (below 1g) but begins to severely under-correct as the mass increases, particularly for the Pu metal lumps.

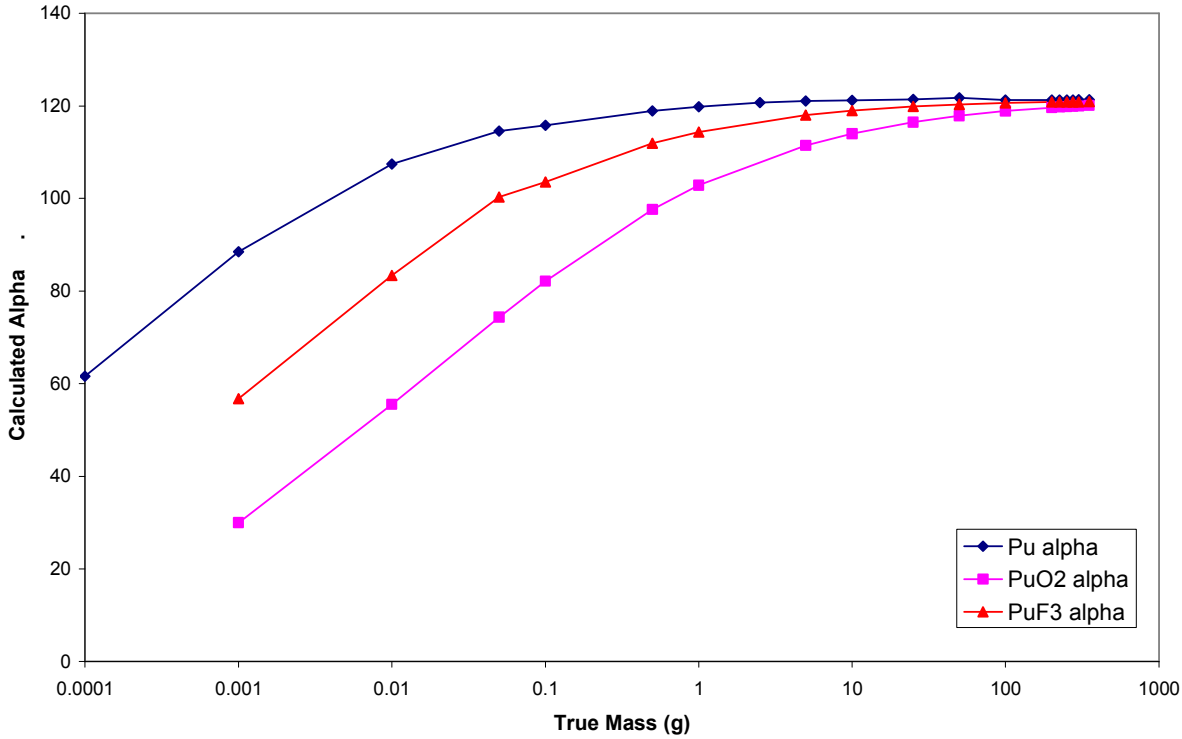

Figure 26: The calculated alpha parameter versus true mass of the lump using the 3-line Fleissner method.

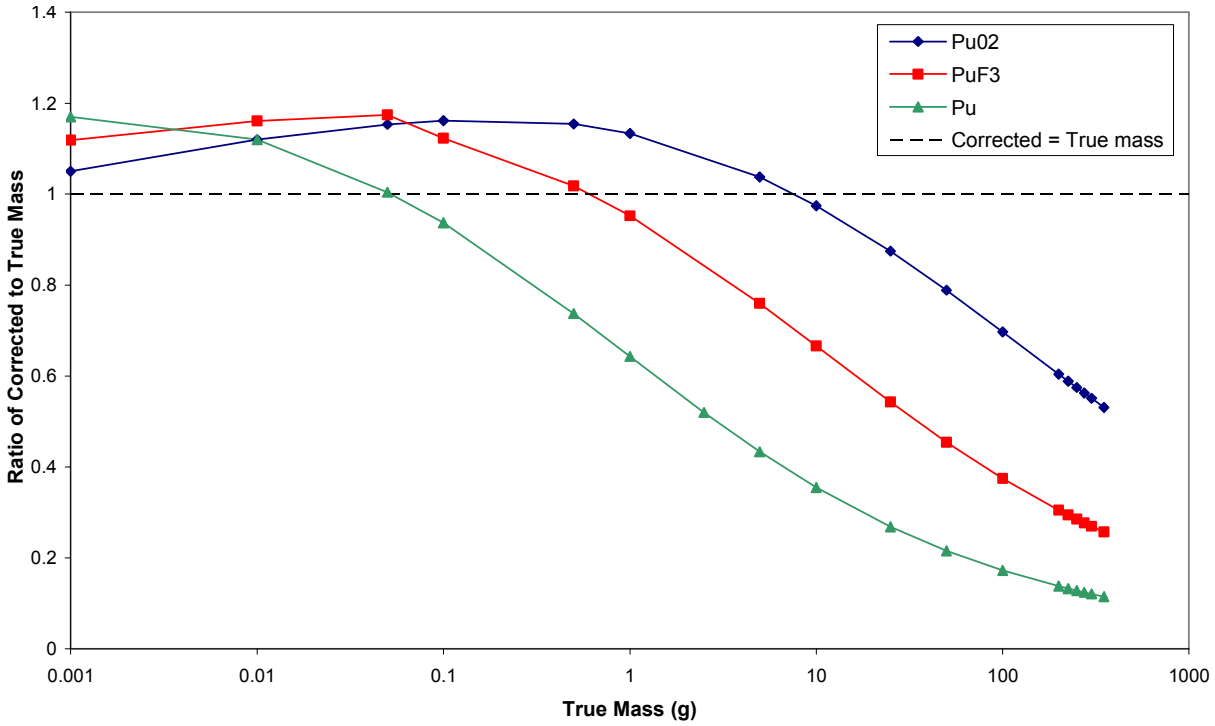

Figure 27: The ratio of corrected to true masses for Pu, PuO_2 and PuF_3 versus true mass for the 3-line Fleissner method.

3.5 General Self-Absorption Analysis

The analysis of the uncorrected behaviour of self-absorption for cylinders has been extended to a number of other rotating geometries over the range 1 mg to 350 g. These are listed below:

- Cylinders with diameter equal to height (as shown above)
- Square faced plates with a fixed depth of 1.0×10^{-3} m and the square side ranging from 2.0×10^{-4} m to 433 mm
- Rods with a fixed length of 0.1 m, with diameters ranging from 2.5×10^{-5} m to 4.9×10^{-2} m
- Cubes of side length ranging 3.0×10^{-4} m to 5.7×10^{-2} m
- Plates of fixed square face length 3.0×10^{-3} m with heights ranging from 5.0×10^{-7} m to 8.4 m
- Plates of fixed square face length 3.0×10^{-2} m with heights ranging from 2.0×10^{-7} m to 0.2 m
- Plates of fixed square face length 0.1 m with heights ranging from 2.0×10^{-7} m to 1.9×10^{-2} m
- Zero attenuation geometry (129 keV mass = 414 keV mass = true mass)

Figure 28 shows M_2 (the apparent mass of the 414 keV line) plotted against M_1 (the apparent mass at 129 keV) for a selection of these materials/shapes with lines of constant true mass in the range 0.001-350 g shown in black, creating an interesting and useful 3D surface whose properties may be used to approximate a more accurate mass based upon the measured (observed apparent) masses of the 129 keV and 414 keV lines.

The diagonal line where M_1 equals M_2 in Figure 28 is the case of no attenuation, where M_1, M_2 and the true mass are all equal in value. It is physically impossible for a lump to produce a data point in the region below this line, although this may be observed experimentally due to statistical fluctuations. The curve at the furthest distance from the no-attenuation line is the case for Pu cylinders (the most attenuating material and shape considered). Tiny massed lumps of Pu that do not experience attenuation will lie on the no-attenuation line. As their mass increases and the 129 keV and 414 keV lines become more attenuated, the curve migrates towards the highest attenuation curve. As the mass increases further they saturate and the points bunch together on the most attenuating line. For a solid, homogeneous, non-re-entrant body the sphere is the worst possible case, however the Pu cylinder is the closest modelled example and so no data point should reside beyond this curve.

Based on this database of calculated results a new Pu SAC method (a software engine) has been developed to calculate the mass of Pu from the two apparent masses M_1 and M_2, and has been used to demonstrate the effectiveness of the new self-absorption technique. This method is described in section 3.7.

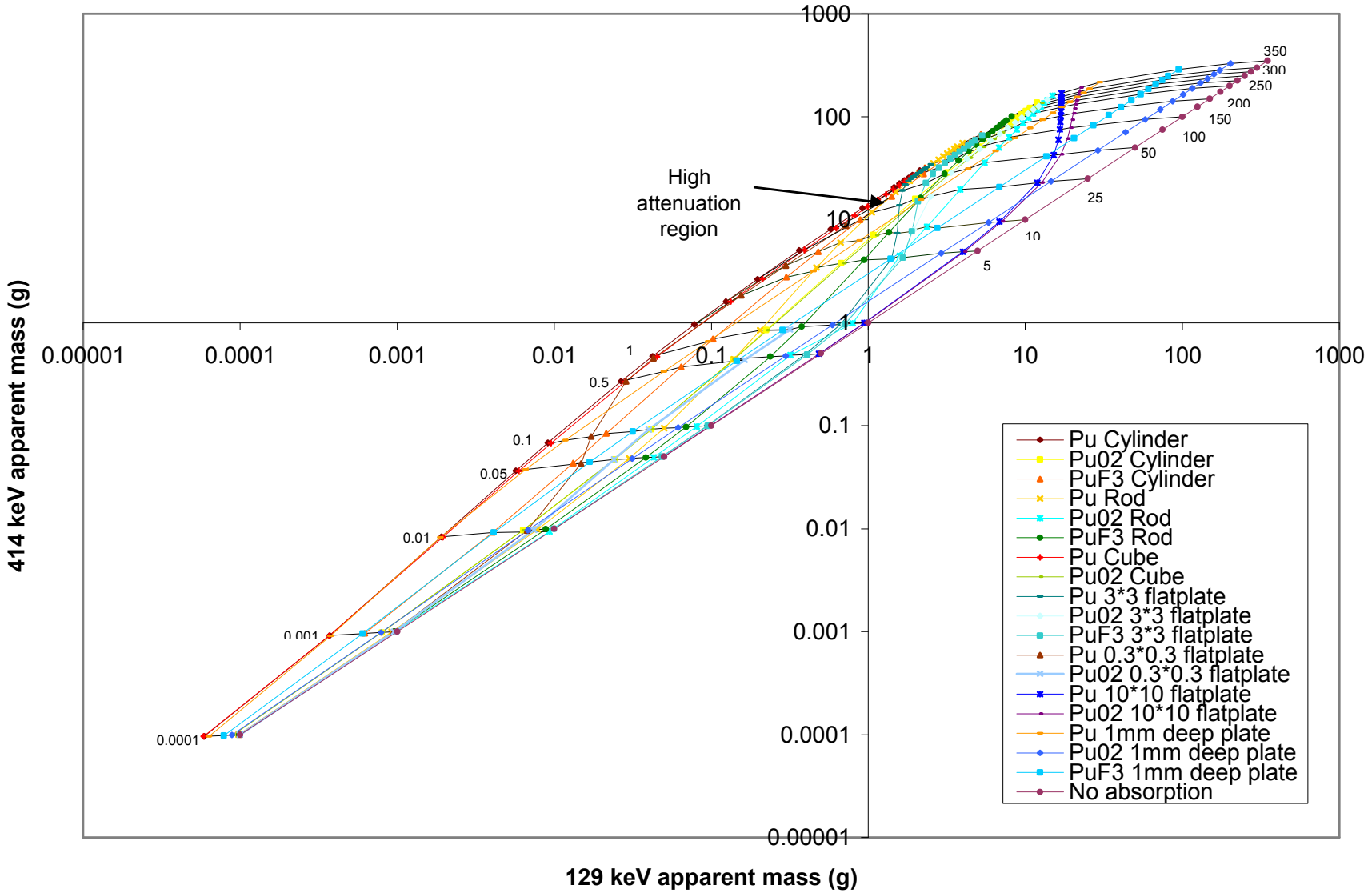

Figure 28: Apparent Masses of the 414 keV Line vs the 129 keV Line.

3.6 Effects of Integration Intervals in Modelling

During the modelling process it was noted that the number of integration intervals used by the point source model has an effect on the resulting counts detected. The model divides the specified lump into a number of voxels, determined by the user-defined number of integration intervals in the relevant dimensions. These are radial, polar and height integration intervals for cylindrical lumps, and lateral, depth, height and rotation integration intervals for cuboidal lumps. The model sets the gamma-ray production in each voxel using the volume of the voxel and computes the probability of the gamma-rays reaching the detector without scattering or absorption.

A study has been performed to observe the effect of the number of integration intervals used by the point source model using a 5 g un-encapsulated cylindrical Pu lump (with diameter equal to height). Each interval dimension (radial, polar, and height, as demonstrated in Figure 29) is varied in turn from 1 to 100, with the remaining interval values set to 100.

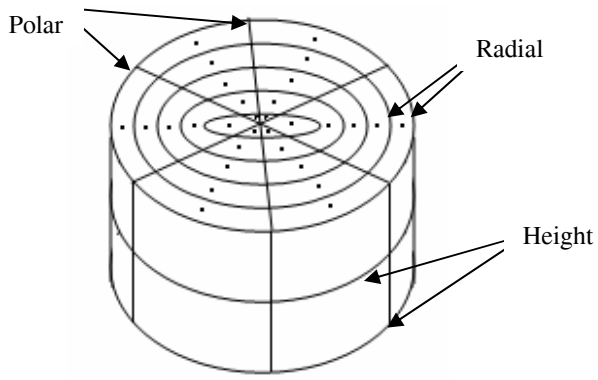

Figure 29: Radial, polar and height integration intervals for a cylinder.

A graph of the apparent mass versus the number of radial integration intervals for the 129 keV line is shown in Figure 30. If the number of intervals is too small and the number of gamma-rays escaping the material decreases exponentially with distance from the edge of the lump, since the absorption is calculated from the centre of the voxel in which the μ is assumed to be constant, the

region of least absorption nearest the edge of the lump is neglected. This causes an underestimation of the apparent mass for too few radial intervals.

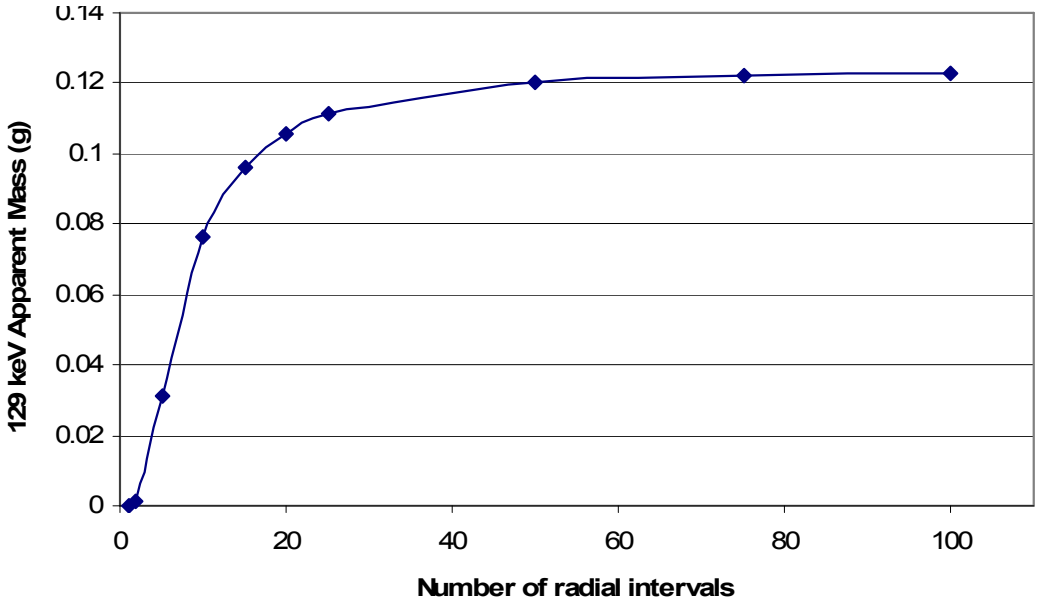

Figure 30: The apparent mass of the 129 keV line for a 5g Pu cylinder as the number of radial intervals is varied.

The number of height and polar intervals do not affect the result as strongly as the radial intervals. These show a slightly fluctuating effect below 10 intervals, and then reach a constant value since for this example each height and polar segment are adequately estimated by this number of intervals. Cylindrical lumps with different masses (modelled for 0.001 g and 20 g lumps) follow a similar pattern as the number of intervals is varied, except that the variation with radial intervals settles more quickly for smaller masses since each voxel is smaller.

During the point source data modelling process, the number of integration intervals was set as large as possible with, for the largest lump, the distance from the centre of the outermost voxel to the edge of the lump set to be much less than $1/\mu\rho$. For example, for the 5g cylinder at 129 keV with a diameter of 0.68cm and a density of 19.8 g/cm^3, the number of radial intervals should be

greater than $\frac{\mu\rho \times diam}{2} \approx 25$. However, whilst determining the number of intervals for a particular lump the modelling time and CPU usage was also a factor which needed to be taken into account. For example, a cylinder with integration intervals of 500-500-500 with two detectors at 99% CPU usage took 21 minutes to complete.

The number of integration intervals used in the model for each set of lump types used for the Pu SAC algorithm has been based upon the largest lump, varying the number of intervals in each dimension so that the counts per second calculated did not vary by more 1%.

3.7 A New Pu SAC Method

In order to use the modelled data to obtain a SAC mass from the two apparent masses, for each material and shape combination modelled in section 0, a cubic spline method has been used to plot curves for the true mass (M_T) versus M_2, and M_1 (129 keV line) versus M_2 (414 keV line), to obtain the self-absorption corrected mass and M_1 as functions of M_2.

Using these splines, for every M_2 we may take a slice of the surface with varying true mass and M_1 and observe a range of (M_1, M_T) pairs which are plotted against one another (see Figure 32). By using the measured value of M_1, and treating the locus between successive points as a straight line, the SAC mass may be found. If the M_2 co-ordinate lies outside the 3D surface, a least squares fit is used with the nearest 4 points.

A software engine has been developed using Borland Delphi™ as a stand-alone Pu Self Absorption Correction engine.

3.7.1 Engine description

The Pu SAC engine was designed to perform as part of a complete assay system; however its main function has been separated so that it can be used for manually inputted values.

The engine requires four values to be inputted. These are the total Pu apparent masses for the 129 keV and 414 keV lines and their uncertainties. If the known masses are for ^{239}Pu then the values must be scaled using the correct ^{239}Pu isotopic value to account for the absorption of the other Pu isotopes, since the model is designed to perform on pure Pu apparent masses.

Due to counting statistics for cases of near-zero attenuation, the 129 keV mass may appear to be slightly greater than the 414 keV line mass. In this case the program will set the two lines' masses to be equal to the 414 keV line mass and will assign no attenuation.

The program tests the limits of the data to ensure there are enough points to perform the calculation correctly. Since the individual materials' curves are fitted only to the maximum point

used in the development stage, the 3D shape is undefined beyond these points (which differ between materials). There must be at least 4 points in order for the program to process the least squares fit, therefore the maximum inputted value of the 414 keV line mass is 216.84 g. Beyond, or equal to this limit the program will set the result to be 216.84 g and the errors become meaningless. However this limit is not an inherent limitation of the general approach just described. It is rather a pragmatic limit set, at this time, by the amount of modelling work undertaken as part of this study to define the 3D surface.

Similarly, there is a minimum limit below which the curve is undefined, which is 0.000097g. Since at very low masses the attenuation is negligible, if the 414 keV line mass is below this value the program will accept the inputted 414 keV mass. In practice the lower limit plays little role since the correction is negligible and the signal will ultimately fall below the detection limits.

The program then uses a cubic spline method based upon that used in J. Wood's "Computational Methods in Reactor Shielding" [51] to obtain curves for M_1 and M_T versus M_2. The inputted 414 keV mass (M_2) is used along with the splines to calculate co-ordinates for a plot of the 129 keV line mass versus true mass i.e. to calculate the co-ordinates of points of a cross-section of the 3D shape for a specific 414 keV line mass. Additionally there is the case of zero-attenuation, where the true mass and 129 keV mass are both equal to M_2.

The next stage of the program uses a series of loops to rearrange the data so that the 129 keV masses (M_1) for each material and their corresponding true masses are in ascending order, using a bubble (or exchange) sorting method [52]. The basic process for this section is to look at each M_1 in turn and test to see if it is greater than the previous, and if so, to move the appropriate array components to place the data in ascending order. The zeroes are filtered to the beginning of the array.

Once the data are correctly ordered the self-absorption corrected mass must be found for the inputted 129 keV line mass from the series of M_2,M_T pairs. An example of this relationship for an M_2 of 5 g is shown in Figure 31.

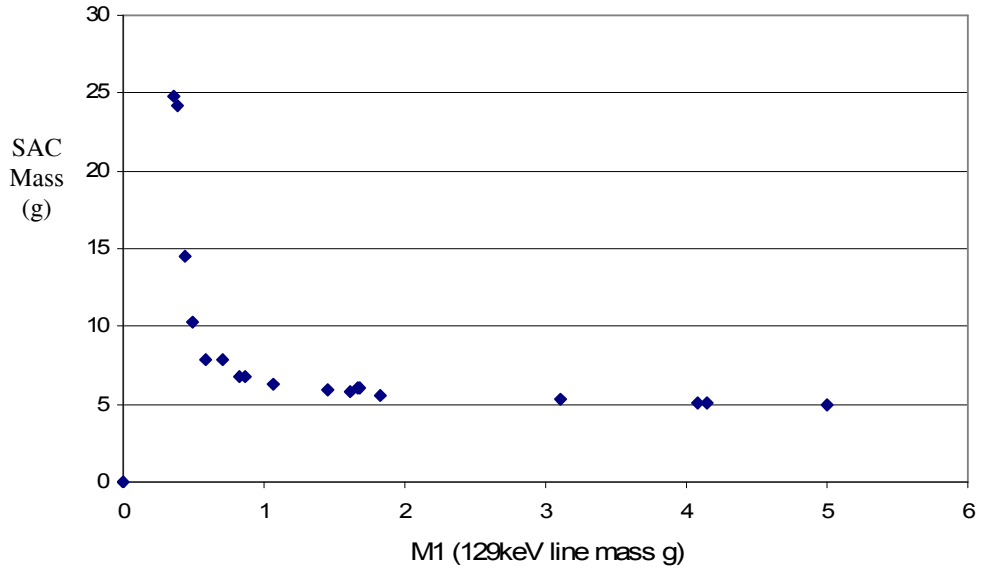

Figure 31: An example of M_1, M_T pairs calculated by the new SAC algorithm for M_2 = 5g.

For the given 129 keV line (1.25 g in this example) the SAC mass must be found. This is done by assuming that the curve joining each two adjacent points is a straight line. We must first therefore, find between which two points the inputted M_1 lies. The SAC mass is then found using the equation of a straight line:

$$SACMass = \frac{M1In.(M_T[n+1]-M_T[n])}{(M_1[n+1]-M_1[n])} + M_T[n] - \frac{M_1[n](M_T[n+1]-M_T[n])}{(M_1[n+1]-M_1[n])} \quad \textbf{Eqn. 19}$$

where *M1In* is the inputted 129 keV line mass, $M_1[n]$ is the array of 129 keV masses for individual materials found from a cross-section of the 3D surface, $M_T[n]$ is the array of true masses for individual materials found from a cross-section of the 3D surface, and [n] and [n+1] are the array components between which the inputted 129 keV mass lies.

If the inputted 129 keV line mass is greater than the largest M_1 on the graph, then a least squares fit is used on the last 4 points, and the line extended to determine the value of the SAC mass. The equation for the least squares fit is shown below.

$$SACMass = M1In \times \frac{\left(4\times\sum M_1 M_T - \sum M_1 \sum M_T\right)}{\left(4\times\sum {M_1}^2 - \left(\sum M_1\right)^2\right)} + \frac{\left(\sum {M_1}^2 \sum M_T - \sum M_1 M_T \sum M_1\right)}{\left(4\times\sum {M_1}^2 - \left(\sum M_1\right)^2\right)} \quad \textbf{Eqn. 20}$$

The uncertainties (one sigma) on the corrected mass arising from the uncertainties in the measured apparent masses, based on the assumption that a single lump is present, have been implemented within the engine using the following equation:

$$\sigma_{M_T}{}^2 = \left(\frac{\delta M_T}{\delta_1} . \Delta M_1 \right)^2 + \left(\frac{\delta M_T}{\delta_2} . \Delta M_2 \right)^2 \qquad \textbf{Eqn. 21}$$

where $\delta_1 = 0.001 \times M_1$, $\delta_2 = 0.001 \times M_2$ and ΔM_n are the inputted uncertainty in the 129 keV or 414 keV masses. Partial differentials are found by propagating small changes in M_1 and M_2 through the calculation process. This equation follows from a standard formula for calculating the standard deviation of summed variables [53], assuming that the variables are uncorrelated and have Gaussian distributions:

$$\sigma_f{}^2 = \sum_i \left(\frac{\partial f}{\partial x_i} \right)^2 \sigma_{x_i}{}^2 \qquad \textbf{Eqn. 22}$$

where f is a function of x_i.

There are small additional uncertainties introduced by the spline fits and interpolation fitting techniques, however, these uncertainties are negligible (for all practical purposes) compared to the uncertainties from the counting statistics etc. and are therefore ignored in the uncertainty determination process at this stage. This issue is discussed in section 3.8.2.

3.8 Effects of Data Fitting Techniques

The first generation Pu SAC algorithm made use of a number of fitting techniques which could be replaced or improved. These are:

- straight line fits between the points on the M_1:M_T pairs
- least squares fits beyond the modelled 3D surface
- polynomial or spline fits to the modelled data

These fitting mechanisms are studied in brief in the following sections.

3.8.1 M_T:M_1 Pair Fitting and Fitting Beyond the 3D Surface

In the Pu SAC algorithm, the M_T:M_1 pair fitting has been performed on the basis that the curve between two adjacent points may be approximated to a straight line. This assumption performs well in most cases where there are numerous points or the gradient is small. However, there may be cases where the data points do not behave predictably due to other fitting techniques used earlier in the modelling process (for example see section 3.8.2) and a cluster may move so that a straight line fit between adjacent points is no longer a good estimation, hence other types for fits may be used to best fit the data.

When a scenario is encountered where the data point would lie beyond the 3D surface, a straight line fit between the nearest four points is used to extrapolate out to the required M_1. This method performs well for larger M_1 values where there are a large number of data points, however it may introduce significant errors in the lower M_1 region, particularly for high mass samples. An example of such a scenario is shown in Figure 32. Due to the clusters of data points and uncertainties that could be introduced from inaccurate modelled data fitting, particularly for higher mass extrapolation, it may be more beneficial to use a curve which represents the trend of the whole set of M_T:M_1 pairs.

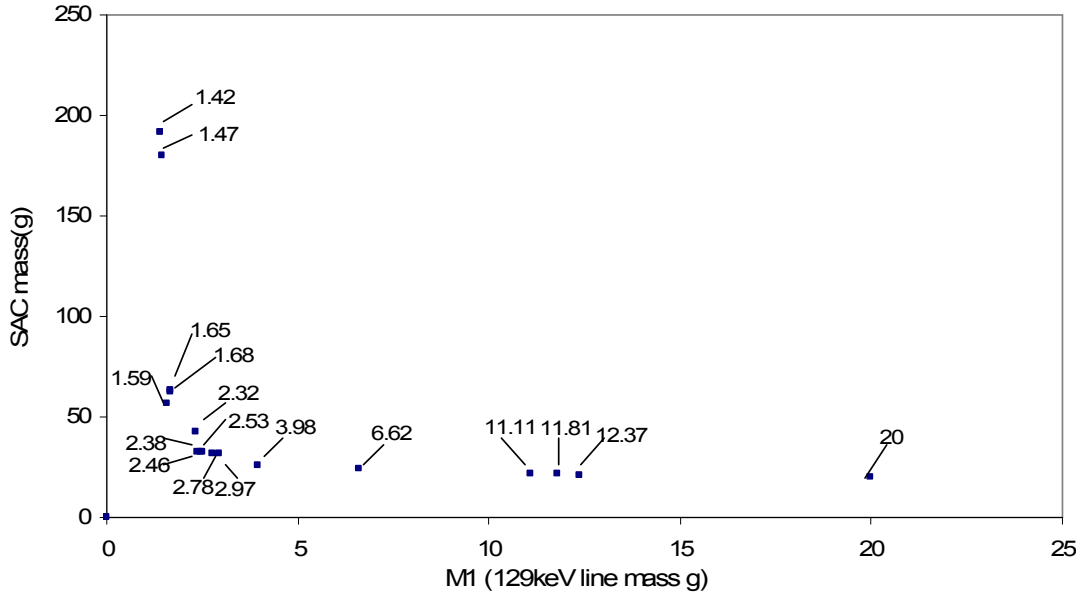

Figure 32: An example of M_T:M_1 pairs for M_2=20g.

An attempt to find a correlation between the coefficients of curve fit equations for M_T:M_1 pairs by plotting the curves for a number of inputted M_2 masses and observing the curve coefficients has been made. This could allow the M_T:M_1 curve coefficients to be calculated within the program algorithm so that no straight line (or other curve) estimations need to be performed by the program. However, the results of preliminary analyses show that the coefficients behave unpredictably and so this would not be possible. Therefore, the algorithm may need to perform an *ad hoc* curve fit.

A number of different methods have been compared in a study to determine the best M_T:M_1 curve fit technique both within and just outside the 3D surface. These are:

(1) a cubic spline method, using the final spline to extend beyond the 3D curve

(2) a straight line fit between adjacent points within the 3D surface and a least squares fit between the 4 end points outside the surface (used in the original Pu SAC algorithm)

(3) an exponential fit to the nearest 4 data points to the required M_1

(4) an exponential fit to the nearest 6 data points

(5) a power law fit to the nearest 4 data points

These 5 methods have been applied for 10 different examples across the range of masses using data modelled for the 1.5 cm cylinder (ρ=10 g.ml^{-3}), 1cm plate (ρ=12 g.ml^{-3}) and 2.5 cm plate (ρ=2 g.ml^{-3}). The ratio of calculated to true mass has been compared across the dataset to observe the average ratio and the standard deviation of the data. The results are displayed in Table 6.

Table 6: Results of M_T:M_1 pair fits using the five investigated methods.

Method	cubic spline(1)	straight line(2)	four-point exponential(3)	six-point exponential(4)	four-point power law(5)
Average ratio	0.14	1.17	1.17	1.10	1.16
Standard Deviation	2.52	0.19	0.31	0.24	0.30

The cubic spline method shows a large spread in results since the fluctuation in position of data points does not behave similarly to cubic equations locally within the constraints (the curve and first derivative must be continuous) and so the algorithm produces widely varying results. The remaining four methods are not constrained in such a way and act as best fit approximations. Each of these methods performs similarly well over the range of data, however the straight line fit produces the smallest spread of results.

Outside the 3D surface each method may suffer since the curves are extrapolated out to the required M_1, highlighting any inconsistencies between fitting methods and the true curve shape. Ideally each M_T:M_1 dataset could be fit to a single curve type for the whole range of lump sizes, however this is not the case since the curves vary too much across the mass range and are not well conditioned. Also since the modelled 3D surface should cover almost all lump shape and density possibilities from the most to least attenuating, any instances of data beyond the 3D surface should be due to counting statistics, matrix corrections, or other small uncertainties and corrections in the inputted 129 keV and 414 keV apparent masses, resulting in minimal deviations from the 3D surface. Consequently a straight line extrapolation from the nearest 4 points should provide a good estimation of the true mass without increasing the complexity of the algorithm. If, however, the Pu SAC method were to be used in a user-driven (as opposed to a fully automated) analysis of the data, a more accurate result could be obtained by fitting the M_1:M_T dataset to an appropriate curve.

3.8.2 Modelled Data Fitting

The first generation Pu SAC algorithm used 6th order log polynomial curves to fit the modelled data in order for the curves to be reproduced in the Delphi program. This fitting technique had originally been used since the trend lines were able to sufficiently fit the data over the mass range with the tools provided (Borland^{TM} Delphi and Microsoft^{TM} Excel) for the purpose of demonstrating the feasibility of the technique. However, other types of curves have been shown to fit the data more accurately, and are consequently used in the resulting engine, as demonstrated in the following sections.

3.8.2.1 Polynomial Fits

The original Pu SAC algorithm that was developed used 6th order log polynomials to fit the modelled data instead of the cubic splines method currently used. The values of M_1 and M_T at each inputted mass have been compared to the original modelled data to illustrate the accuracy of these 6th order log polynomial curves. Although the majority of the curves show errors of less than 1%, some curves such as the rods and flat plates which are more difficult to fit, show errors of up to 11% for M_T and the rods up to 22% for M_1. Note that the 0.3x0.3cm Pu flat plate and the Pu and PuF_3 3x3cm flat plates were omitted from the first generation algorithm since their curves fits using this method were not accurate and introduced additional uncertainties.

It was observed that the curves do not fit the data well over the entire range and so the data were been split into two sets for the lower (0.0001 g-50 g) and higher (50 g-350 g) masses to allow the curves to be fitted more easily. Each half has been fitted to obtain equations for $M_T(M_2)$ and $M_1(M_2)$ and the errors have been determined.

An alternative method to improve the fits would be to use a different order of polynomial. The 6th order log polynomial, which fits the majority of the data relatively accurately, could be increased to a higher order log polynomial, for example a 10th order log polynomial. This has been performed using Oakdale Engineering's Datafit^{TM} program [54].

The 3x3 cm Pu flat plate and 10 cm PuO_2 rods have been selected to demonstrate different fitting techniques since these curves represent the largest errors for M_T and M_1 respectively.

Table 7: Summary of errors for sample modelled data fits.

Method	3x3 cm Pu flat plate				10 cm PuO_2 rod			
	Avg M_T error %	Max M_T error %	Avg M_1 error %	Max M_1 error %	Avg M_T error %	Max M_T error %	Avg M_1 error %	Max M_1 error %
6^{th} order log polynomial	4.12	11.20	0.67	2.93	0.40	2.09	3.88	22.10
Dual 6^{th} order log polynomials	0.17	0.82	0.21	2.93	0.32	1.99	2.39	16.77
10^{th} order log polynomial	1.55	3.97	0.52	1.24	0.24	1.23	2.90	13.59
Dual 10^{th} order log polynomials	0.15	0.82	0.06	0.32	0.20	0.97	2.23	10.41

The results for the original and different fit techniques described above are summarised in Table 7 in the first three rows. The effect of splitting the curve in half evidently improves the data fit to some extent. It may be possible to split the data sets into numerous curve fits to reduce the fitting errors further, however this would increase the complexity of the program algorithm.

Each technique reduces the errors in the fitted data, however the dual fit is better for the 3x3 Pu flat plate whereas the 10^{th} order log polynomial produces the better fit for the 10 cm PuO_2 rod. These two methods have been combined so that the data are fitted with two higher order log polynomials. 10^{th} order polynomials were not always possible due to the there not being enough data points to fit in each half, and so the largest order polynomial is used in each case. The results are listed in the last row of Table 7, showing an improvement from the original 6^{th} order polynomial fits.

Although the above polynomial fitting methods reduce the errors at each point, it is possible to use an alternative fitting technique so that this error becomes zero, such as a cubic spline fitting method. This alternative shall now be considered.

3.8.2.2 Cubic Spline Fits

A cubic spline interpolation uses a continuous, smooth piecewise curve between the data points using separate third-order polynomial fits for each section. One condition of the function is that it will interpolate all entered data points so there will be no error from the original data, unlike the polynomial fitting method. The cubic spline method fits the data points but in between there will still be an interpolation error. This has been tested below.

A program has been written in Delphi^{TM} to create a cubic spline fit for n data points and evaluate the y-value of any given x-co-ordinate within the range of inputted x-co-ordinates. This program has been based upon a method used in J. Wood's "Computational Methods in Reactor Shielding" [51]. The spline algorithm has been implemented within the Pu SAC program, replacing the polynomial fit method, and tested using the following three lump types over the mass range 0.0001 g-350 g:

- 1.5 cm high cylinder with a Pu density of 10 $g.cm^{-3}$
- 1 cm high plate with a Pu density of 12 $g.cm^{-3}$
- 2.5 cm high plate with a PuO_2 density of 2 $g.cm^{-3}$

The spline technique demonstrates an overall improvement from the polynomial methods in the intermediate and high-mass regions. The results are illustrated in Figure 34.

3.9 Modelled Results

The developed Pu SAC method (using cubic spline fitting) has been compared to the basic 2-line and 3-line (unconstrained) Fleissner SAC methods in Figure 33 by inputting the original modelled data (from which the algorithm was created) for a mass range of 1 mg to 250 g, the upper value of which can be considered to be an extreme range for a single lump in most waste assay scenarios. The new engine for this data provides a SAC mass which is much closer to the true mass than the Fleissner techniques, excepting the final 350 g points where the ratio of corrected to true mass is significantly low/high.

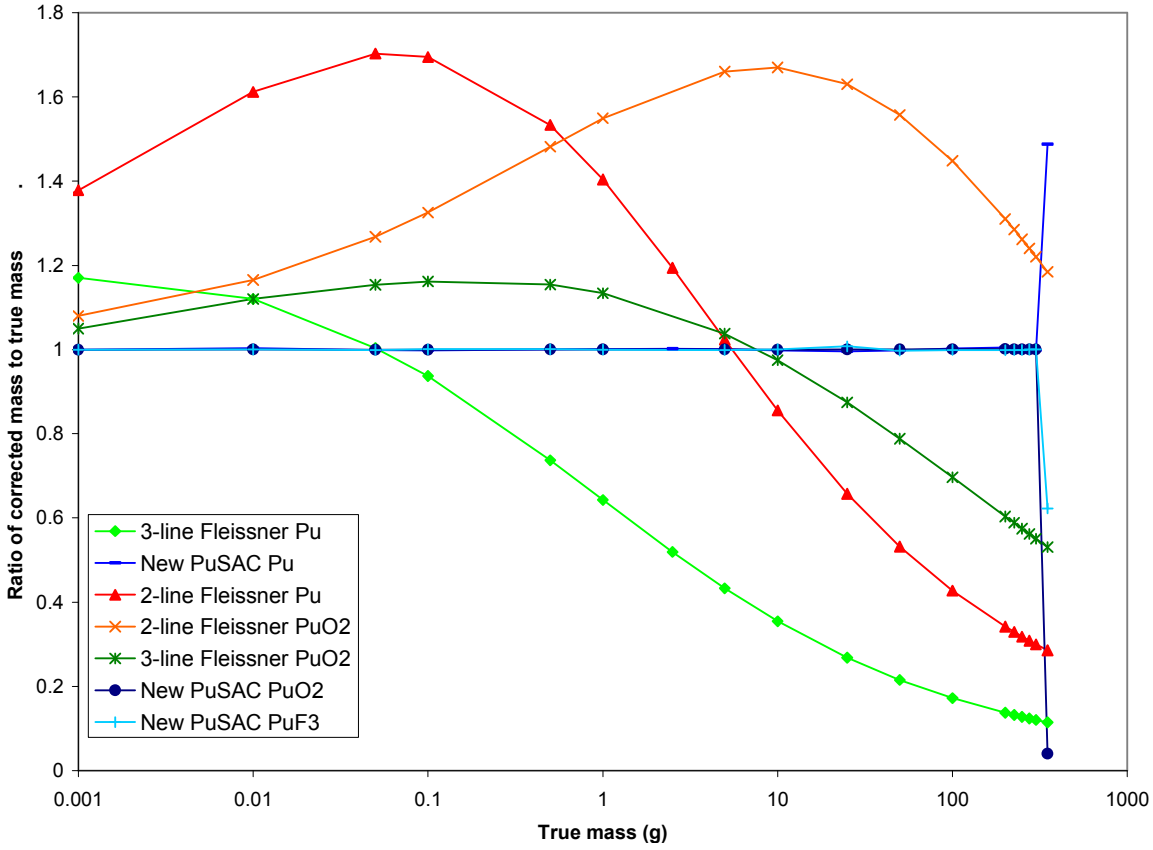

Figure 33: Comparison between the Fleissner SAC method and the new SAC algorithm results.

At 350 g the lump has become highly attenuating. In fact, the modelled data produces a point on the M_1:M_T graph that is beyond the most attenuated modelled point i.e. a co-ordinate outside the

limits of the 3D surface. Consequently the algorithm uses a linear least squares fit of the nearest (most attenuated) four modelled points and extrapolates to the inputted M_1. The fitting technique has been investigated in more detail in Section 3.8.1.

The above comparison is unrealistic because it re-uses the data that originally created the numerical model resulting in 'incestuously' over-optimistic results, where each M_2 will lie exactly at a modelled point, and will create a set of M_1:M_T pairs that all lie exactly on or very close to modelled data points. Consequently the effects of using 6^{th} order log polynomials as trend lines and using the straight line fit between M_1:M_T pairs is not tested sufficiently.

Consequently, the algorithm has also been tested with modelled data from three new lump types that were not used as input for the curves in the new algorithm. These are:

- 1.5cm high cylinder with a Pu density of 10 $g.cm^{-3}$
- 1cm high plate with a Pu density of 12 $g.cm^{-3}$
- 2.5cm high cylinder with a PuO_2 density of 2 $g.cm^{-3}$

The lumps have been modelled with a mass range of 0.1 mg to 350 g and are compared to the basic 2-line Fleissner method, along with the 6^{th} order log polynomial result, as described in section 3.8.2.1 (see Figure 34).

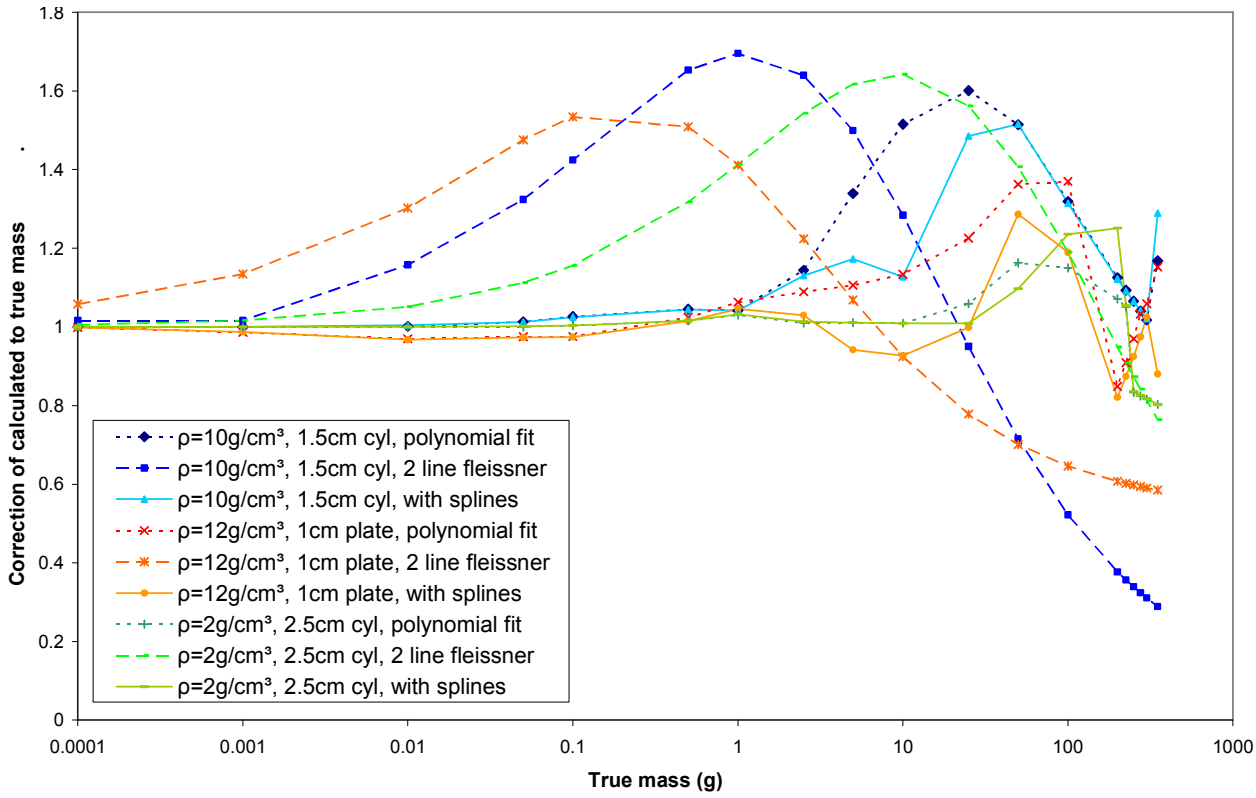

Figure 34: Graph showing the calculated to true mass ratio comparison using the polynomial and spline Pu SAC, and the 2-line Fleissner methods for new modelled lumps.

Figure 34 shows that the spline method fits equally as well as the 6th order log polynomial method at the lower (up to 1 g) and higher (above 100 g) mass regions, but performs better than the polynomial method in the intermediate region (between 1 and 50-100 g). The spline method has shown an improvement to the first generation (polynomial fit) Pu SAC algorithm in the intermediate region, however the lack of improvement in the higher mass region is due to the modelled data points themselves rather than their fitting technique. The high mass data used in Figure 34 are for greatly attenuating lumps that are located within the clustered region of the (M_1:M_2:M_T) 3D surface. Within this region the lumps begin to saturate (only the surface of the lump is detected- the apparent mass is proportional to the projected area) and the surface effects of the sample (which vary with the shape of the lump) dominate. Consequently the 3D surface appears less well behaved since the points to not lie on smooth constant true mass curves and the Pu SAC algorithm becomes limited (see section 3.10).

The new PuSAC engine with splines demonstrates much improved results (i.e. the ratio of corrected to true is closer to unity) than the 2-line Fleissner method for lumps up to 5 g, but larger lumps drift up to a ratio = 1.3 line whereas the Fleissner method begins to underestimate. On comparison of the data and Figure 28, the Pu SAC algorithm produces less correct results in the regions of high attenuation, where the data points appear to be denser. This region of the graph (the most attenuating region) will suffer from worse errors than the less attenuating side of the 3D surface since the lines of constant M_T are much more compact and the M_1:M_T graph becomes very steep, hence a small change in any of the input parameters will result in a large change in calculated M_T.

It can be appreciated that at low masses the counting precision may be limiting but that the corrections are relatively small. As noted above the 414keV apparent mass may be an adequate default value for the true mass. At high masses on the other hand the lump may be close to saturation, meaning that only the surface regions are viewed and that a large fraction of the mass plays little part in the measurement. In this case the statistical accuracy may appear to be much better, but by the same token the demands on the data to distinguish different massed bodies based on small fractional changes in size is also increased.

The UK ILW/LLW Pu limit for a 60 kg gross weight drum (~40 kg net weight) is in the range of 50-90 mg depending on the isotopics and the new SAC technique is seen to work accurately without over-reporting in this range which will significantly improve sentencing. The fluctuations at higher masses are discussed more fully in section 3.10.

3.10 PuSAC Limitations, the Number of Modelled Points & the High Attenuation Region

The number of lumps and densities used for the algorithm has been limited purely by the capabilities of the point source model and CPU time. The original Pu SAC algorithm has been modelled using 7 different shapes and up to 3 densities, resulting in 19 separate lump/density combinations. Also, a number of these lumps were subject to limitations caused by the minimum input lump dimensions in the point source model and the maximum size of the lump dimensions in terms of its view from the modelled detector. Consequently some shapes do not have modelled data points across the whole range of masses; although the available lump data have proved satisfactory to demonstrate the Pu SAC method.

The number of data points could be increased by introducing intermediate densities or different shaped lumps if required. This would improve the final true mass result by increasing the number of data points available to perform the M_1:M_T curve interpolation and extrapolation. In the low attenuation region an increase in the number of points would have less of an effect since the results follow a well-conditioned shallow curve, where a small change in M_1 creates a relatively small change in M_T. However in the more attenuating region a larger number of data points would be more beneficial since the data are more erratic.

Where the apparent M_1 lies outside the 3D surface the extrapolated true mass could also be improved. An example is shown in Figure 35 for an M_2 of 3 g. The red points are the original modelled data used for the Pu SAC analysis in the previous sections. The blue points are the three additional lump types modelled to test the Pu SAC algorithm. The two lines (dotted and dashed) show the projected straight line fits between the end 4 points that would be used for an extrapolation with and without the additional lump data. For an M_1 just 0.1 g outside the 3D surface in this case the additional data would change the resulting M_T by 1.5 g.

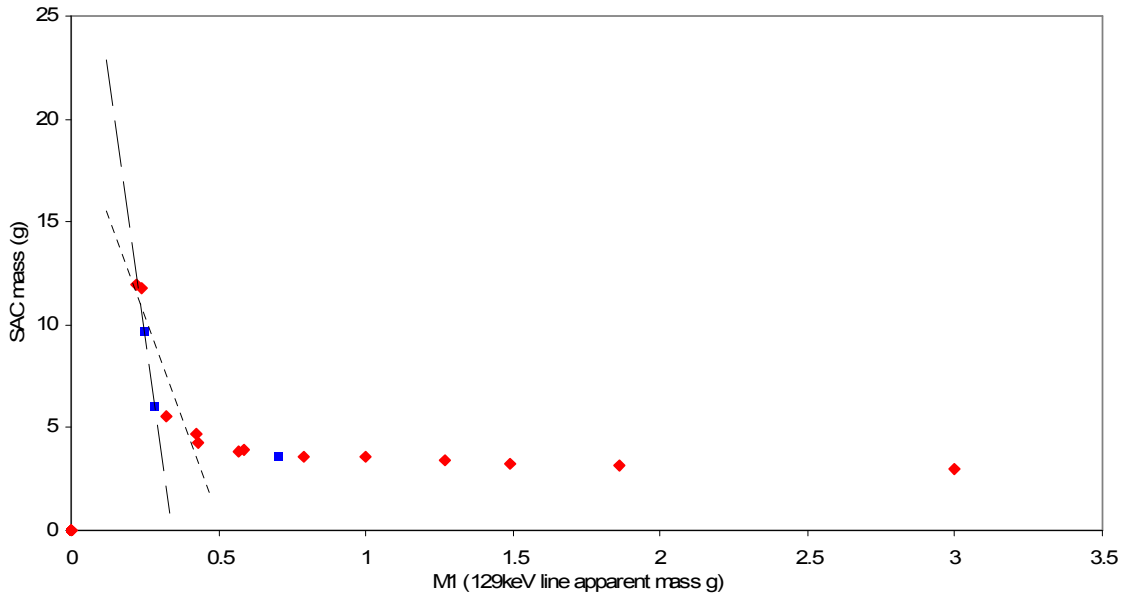

Figure 35: M_1:M_T curve for M_2=3g with additional data to demonstrate the effect of the number of modelled data points.

One disadvantage of greatly increasing the number of modelled points is that if the points were to cluster very close together in the high attenuation region the straight line fit for extrapolation could become a representation of the four data points locally, rather than providing a suitable approximation for high attenuation end of the curve. In this case the least squares fit should be calculated from a larger number of data points.

3.10.1 Material and Shape Dependence

As previously stated, in the high mass area the data seem less well behaved. This may be because as the lumps saturate they behave differently for different shapes and material types. A simple study has been performed to test this using non-rotating cubes and cuboidal flat plates (with side length ratios x, 10x and 15x, with the 10x dimension leading away from the detector). Using a far field approximation the two apparent 129 keV and 414 keV masses for both shapes have been determined by integration over the sample. This has been performed using the SAF as the ratio of the number of gamma rays detected with an absorber to the number detected without an absorber present i.e. for a cuboidal lump viewed in the far field perpendicular to the surface:

$$SAF = \frac{N_{withAbs}}{N_{\mu=0}} = \frac{\int_0^x A\upsilon e^{-\rho\mu x} dx}{A\upsilon x} = \frac{\left(1 - e^{-\mu\rho x}\right)}{\mu\rho x} \qquad \textbf{Eqn. 23}$$

where ν is the specific activity of the sample, N is the number of gamma rays detected, ρ is the density of the sample, μ is the attenuation coefficient and A is the area of the face of the shape normal to the observer. This has been performed for a range of densities for the three materials: Pu, PuO_2 and PuF_3. The results have shown that a 3D surface containing data for one lump shape but all material types suffers from the same effects in the high attenuation region. However, if data are modelled for a single shape and material type for a large range of densities the results follow well conditioned curves in all regions of the 3D surface.

The data for Pu cubes for a range of densities (0.5-19.8 g/cm^3) and masses (0.0001-350 g) have been calculated and used as the basis of a test Pu SAC algorithm using cubic spline M_1:M_2 and M_T,M_2 fits and straight line interpolation between adjacent points on the M_1:M_T curve.

A range of masses between inputted data points for Pu cubes have been input into this test algorithm. The results for Pu cubes for a density of 5 g/cm^3 (used as input for the model) performs very well with corrected to true mass ratios between 1.005 and 0.999. A density of 12 g/cm^3 also performs well with a slowly increasing ratio until a maximum of 1.16 at higher masses. The largest tested true mass was 333 g which gave the minimum ratio of 0.84 since the data were outside the surface.

PuO_2 cubes were also tested using the Pu cube M_1:M_T:M_2 data. The results were that the SAC masses were always less than the true masses, with deviations increasing with true mass until ratios of 0.662 for 5 g/cm^3 and 0.409 for 12 g/cm^3. This is because the apparent 129 keV and 414 keV masses were for PuO_2 (rather than Pu metal as the model expects). The PuO_2 has a lower mass attenuation coefficient μ and is less attenuating; consequently the apparent masses for the 129 keV line are relatively higher, causing a lower true mass than would be determined from an algorithm designed for the correct material type.

From this study it can be seen that the Pu self-absorption correction may be improved if more information is known about the Pu being assayed e.g. its composition and shape; however this is not readily available in nuclear waste assay. The correction may be refined however if limited information is available. For example, if the material is one of only a few possible types, an engine could be created with the appropriate data and a result obtained for each material type, using the difference in results to obtain an improved uncertainty calculation.

3.11 Extension to Multiple Lumps using Modelled Data

Due to the high degree of non-linearity observed in the model, the combination of the apparent masses from a series of smaller lumps was expected to produce a smaller self attenuation factor than that expected for a single large lump of equal true mass. Therefore the model was expected to underestimate the total Pu in the combined-lump sample.

The apparent 129 keV and 414 keV masses for a number of material/shape combinations were summed and used as input for the algorithm to see how it would behave for multiple lumps. These combinations include several lumps of the same material and shape, plus random mixed numbers and types of lumps selected from the range of masses, shapes and material types studied in the Pu SAC algorithm development, plus a series of newly modelled data sets for 1.5 cm high cylinders with a Pu density of 10 $g.cm^{-3}$ and 2.5 cm high cylinders with a PuO_2 density of 2 $g.cm^{-3}$. The results are presented in Figure 36 in a plot of the corrected to true mass ratio versus the apparent 414 keV mass of the lump combination.

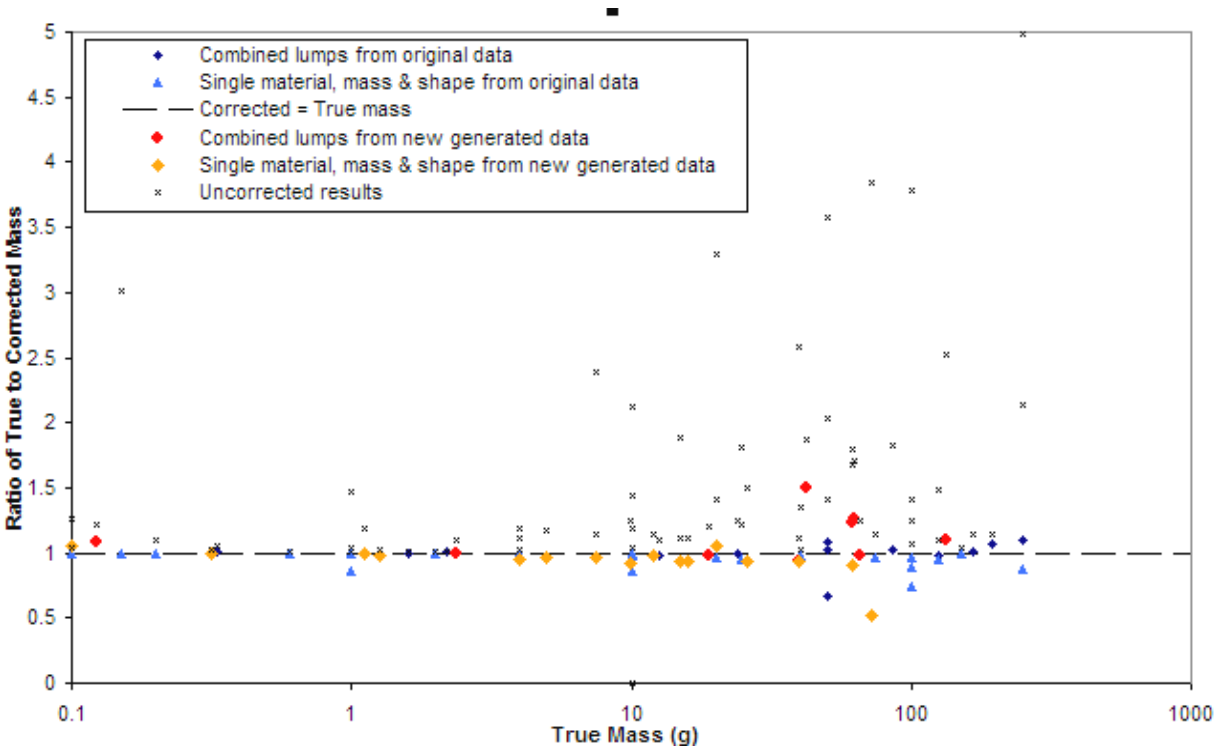

Figure 36: Plot of the ratio of true to corrected mass versus the total true mass for random combinations of lumps collated from independently-treated single lump modelled data.

The uncorrected 414 keV apparent masses are also plotted as a comparison. The results do not produce perfect ratios of one, as expected, because as the individual lumps are combined their total 129 keV apparent mass will be higher than that of a single lump of equivalent mass, whereas the 414 keV apparent mass will remain relatively similar. Consequently the corrected mass of the combination of lumps is underestimated, demonstrated by approximately 80% of the Pu SAC corrected data points in Figure 36. The remaining corrected masses lie above the line where the ratio equals one. This is due to fluctuations in the data points in the high attenuation region of the M_1:M_2:M_T plot.

It should be noted that these lump combinations have been performed by summing the apparent masses of individual lumps, assuming that all lumps are independent and the gamma rays from each lump are not attenuated by any other lump on their path to the detector. However this may not be the case in real waste drums and the resulting apparent mass may be attenuated more than for the examples shown above.

As shown, the method appears to work well for multiple lumps of various compositions. All of the modelled results are within 50% of the corrected equal to true mass line, with 64.3% of the modelled results achieving values within 5% of the true mass. These observations could be developed with a more detailed study to implement a contribution to the Total Measurement Uncertainty (TMU) of the sample from the Pu self-absorption in the case of multiple lumps. For example, if a 1 sigma uncertainty is required by the user (68% of the results should lie within the area if a Gaussian distribution is used, for example), this equates to a 6% uncertainty if the uncertainty is assumed to be constant across the mass range.

It may also be observed that the variation from the corrected equal to true mass line appears to increase with increasing true mass and so the TMU contribution from multiple lumps could be refined to be a function of the apparent mass with a more in-depth study.

3.12 Comparison to other Pu SAC techniques for Modelled Data

The new Pu SAC method has been compared to uncorrected results and the 2-line Fleissner method in section 3.9. This section extends the comparison to other Pu SAC techniques, such as the 3-line Fleissner method with unconstrained parameters and infinite energy extrapolation method using both linear and 2nd order polynomial fits for three lump types:

- Set 1: 1.5 cm high cylinder with a Pu density of 10 $g.cm^{-3}$
- Set 2: 1 cm high plate with a Pu density of 12 $g.cm^{-3}$
- Set 3: 2.5 cm high cylinder with a PuO_2 density of 2 $g.cm^{-3}$

The results are displayed in Figure 37 along with the uncorrected 414 keV line apparent mass.

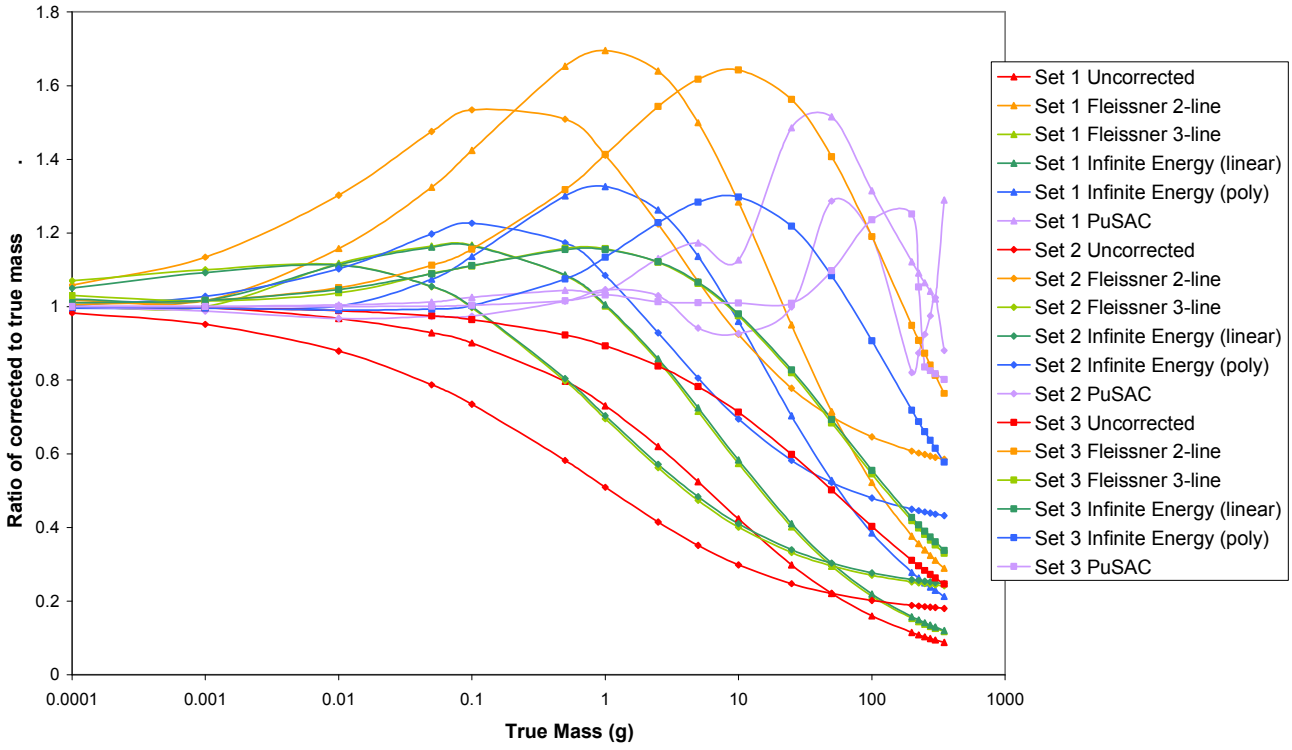

Figure 37: A graph showing the ratio of modelled corrected to true mass for three new lump shapes and materials using the 2-line Fleissner and unconstrained 3-line Fleissner methods, the Pu SAC method plus the Infinite Energy method using linear and polynomial fits.

As noted previously, the Fleissner methods overestimate at intermediate masses and underestimate at higher masses. The linear Infinite Energy Extrapolation methods follow the same curve as the 3-line Fleissner method, whereas the 2^{nd} order polynomial fit to the Infinite Energy Extrapolation method follows a similar pattern to the 2-line Fleissner method but to a lesser extent, offering an improved performance at intermediate masses (with a maximum over-correction of 1.2) but a similar under-correction at higher masses. For the selection of lumps studied above the Pu SAC method shows a clear improvement compared to the other methods across the whole mass range despite the fluctuations at the higher masses (as discussed in section 3.10).

3.13 Comparison to other Pu SAC techniques for Measured Data

The new Pu SAC method has been compared to the other Pu SAC techniques, such as the 3-line Fleissner method with unconstrained parameters and infinite energy extrapolation method using both linear and 2nd order polynomial fits for the AE4043/nn sources measured on the bench in two different orientations. The experiment was set-up using single 70mm diameter by 20mm thick BEGe3820 detector, as described in section 3.3.1. The sources have been measured twice for two different orientations with the source positioned upright (two sets of measurements) and laid horizontally inside the Pb shield, resulting in 4 measurements for each source, as shown in Figure 11.

The raw apparent mass results of these measurements could not be used as a fair representation of the SAC methods since the sources are encapsulated within 2.5 mm of stainless steel. Therefore a correction factor has been introduced to account for the encapsulation. This correction factor has been calculated by modelling the sources in the two orientations for each required energy, and using the ratio of the countrate observed with and without the encapsulation. The XCOM μ with coherent scattering has been used in the ratio calculation, as discussed in section 3.3.4. Due to the limitation of the model the horizontal orientation sources have been modelled as cuboidal sources, of equal mass and surface area perpendicular to the detector as the source itself, contained inside a 2.5 mm stainless steel encapsulation. The upright orientation correction factor has been modelled using the set-up described in section 3.3.4.

The measured results after taking account of the encapsulation are displayed in Figure 38 along with approximate uncertainties and polynomial trend lines for the datasets.

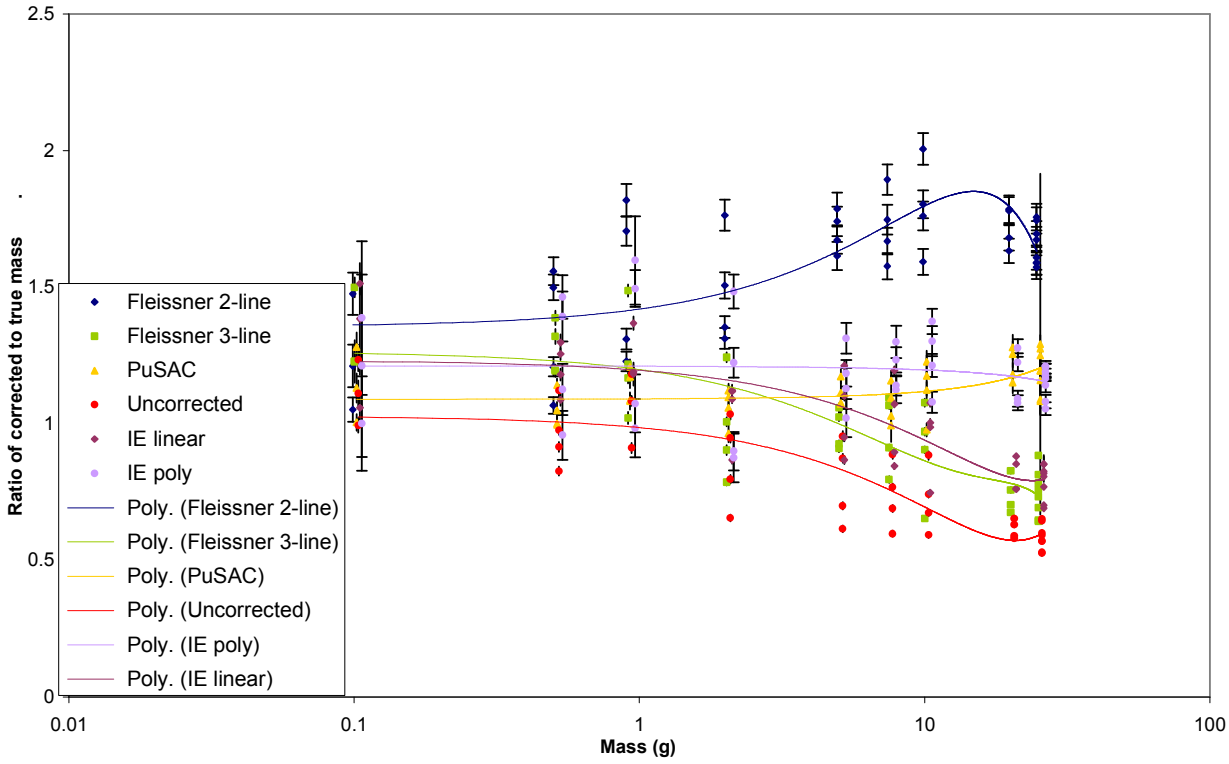

Figure 38: A graph showing the ratio of modelled corrected to true mass the AE4043/nn sources measured in 2 orientations using the 2-line Fleissner and unconstrained 3-line Fleissner methods, the Pu SAC method plus the Infinite Energy method using linear and polynomial fits.

The graph shows the general trend of the corrected Pu mass results in relation to the true unencapsulated mass of the sample. The 2-line Fleissner method has been found to be the least satisfactory across the range of masses, increasing to a maximum of 100% overcorrection at higher masses. The 3-line Fleissner and infinite energy extrapolation with a line fit both overcorrect slightly up to a mass of around 5 g then begin to underestimate the true mass.

The infinite energy extrapolation method with a 2nd order polynomial fit and the new Pu SAC technique both perform very well, with a slight overcorrection across the range of masses, but greatly improving the result compared to the uncorrected 414 keV apparent mass. The results from these two methods are displayed separately in Figure 39.